

Advanced Characterization Methods for Electrical and Sensoric Components and Devices at the Micro and Nano Scales

Evgeniya Sheremet, Peter Meszmer, Thomas Blaudeck, Susanne Hartmann, Christian Wagner, Bing Ma, Sascha Hermann, Bernhard Wunderle, Stefan E. Schulz, Michael Hietschold, Raul D. Rodriguez,* and Dietrich R. T. Zahn

The present study covers the nanoanalysis methods for four key material characteristics: electrical and electronic properties, optical, stress and strain, and chemical composition. With the downsizing of the geometrical dimensions of the electronic, optoelectronic, and electromechanical devices from the micro to the nanoscale and the simultaneous increase in the functionality density, the previous generation of microanalysis methods is no longer sufficient. Therefore, the metrology of materials' properties with nanoscale resolution is a prerequisite in materials' research and development. The article reviews the standard analysis methods and focuses on the advanced methods with a nanoscale spatial resolution based on atomic force microscopy (AFM): current-sensing AFM (CS-AFM), Kelvin probe force microscopy (KPFM), and hybrid optical techniques coupled with AFM including tip-enhanced Raman spectroscopy (TERS), photothermal-induced resonance (PTIR) characterization methods (nano-Vis, nano-IR), and photo-induced force microscopy (PIFM). The simultaneous acquisition of multiple parameters (topography, charge and conductivity, stress and strain, and chemical composition) at the nanoscale is a key for exploring new research on structure-property relationships of nanostructured materials, such as carbon nanotubes (CNTs) and nano/microelectromechanical systems (N/MEMS). Advanced nanocharacterization techniques foster the design and development of new functional materials for flexible hybrid and smart applications.

1. Introduction

Material properties at the nanoscale strongly define the overall system performance of devices. This becomes even more critical with the downsizing of the device scales in our hunt for better, smaller, faster, and more efficient technology. For example, single defects in semiconducting carbon nanotubes (CNTs) or local functionalization can affect the thermal^[1] and electrical conductivities^[2] as well as their optical properties.^[3] Spatial confinement defines the optical properties of the semiconductor quantum dots^[4] as well as the electronic properties of nanowires^[5] or thin-layered materials such as graphene nanoribbons. [6] For sensing applications, the nanoscale properties have important implications for the sensor performance involving micro and nanosystems as outlined, e.g., by de Santiago et al.^[5] for harmful gas detection. Ultimately, any device

Prof. E. Sheremet, B. Ma School of Physics Tomsk Polytechnic University Lenin ave. 30, 634028 Tomsk, Russia

Prof. E. Sheremet, Prof. M. Hietschold Professorship of Solid Surfaces Analysis Chemnitz University of Technology Reichenhainer Str. 70, 09126 Chemnitz, Germany

Prof. E. Sheremet, Prof. R. D. Rodriguez, Prof. D. R. T. Zahn Professorship of Semiconductor Physics Chemnitz University of Technology Reichenhainer Str. 70, 09126 Chemnitz, Germany E-mail: rodriguez@tpu.ru

Dr. P. Meszmer, Prof. B. Wunderle Professorship of Materials and Reliability of Micro Systems Chemnitz University of Technology 09126 Chemnitz, Germany

 $^{[+]}$ Present address: Institute of Ion Beam Physics and Materials Research, Helmholtz Center Dresden-Rossendorf, Bautzner Landstraße 400, 01328 Dresden, Germany.

The ORCID identification number(s) for the author(s) of this article can be found under https://doi.org/10.1002/pssa.201900106.

DOI: 10.1002/pssa.201900106

Dr. T. Blaudeck, S. Hartmann, Dr. C. Wagner^[+], Dr. S. Hermann, Prof. S. E. Schulz
Center for Microtechnologies (ZfM)
Chemnitz University of Technology
Reichenhainer Str. 70, 09126 Chemnitz, Germany

Dr. T. Blaudeck, Dr. S. Hermann, Prof. S. E. Schulz Department of Back-End-of-Line Fraunhofer Institute for Electronic Nano Systems (ENAS) Technologie-Campus 3, 09126 Chemnitz, Germany

S. Hartmann, Dr. S. Hermann, Prof. S. E. Schulz, Prof. R. D. Rodriguez, Prof. D. R. T. Zahn
Center for Advancing Electronics Dresden (cfaed)
Chemnitz University of Technology
Reichenhainer Str. 70, 09126 Chemnitz, Germany

Dr. C. Wagner Professorship of Scale-bridging Materials Modeling Chemnitz University of Technology Reichenhainer Str. 70, 09126 Chemnitz, Germany

Prof. R. D. Rodriguez School of Chemical and Biochemical Technologies Tomsk Polytechnic University Lenin ave. 30, 634028 Tomsk, Russia



performance is largely defined by electrical and (opto)electronic properties, mechanical, and chemical structure of the components at the nanoscale.

We have opted to illustrate the nanoscale characterization capabilities using CNT-based devices. From the classes of nanostructured materials, CNTs have gained interest as the discovery of this material Iijima et al. like the multi-walled CNTs ("helical microtubuli of graphitic carbon")^[7] and single-walled CNTs (SWCNTs).[8] In the following, usage of this material as nanoscale conductor^[9] and (even all-carbon) electronic and sensoric devices^[10] was soon anticipated. In the present article, we will highlight the developments in nanocharacterization for CNT and CNT-based devices for 1) CNT-based vertical interconnects, or vias (vertically aligned CNTs acting as nanostructured conductor); 2) CNT-based field-effect transistors (CNTFETs) with CNTs as planar semiconducting transistor channel; and 3) monolithic microelectromechanical systems (MEMS) with mechanical interfaces to integrate CNTs and other nanomaterials in hybrid NEMS. The latter can even act as an entirely new class of test platforms for the micro-nano interface. [11-14]

Similar to fabrication, technology develops to accommodate the demands of the new devices, and the characterization methods evolve to keep up with measuring the nanoscale properties that allow determining new applications as well as making technological improvements. In many cases, well-developed macroand microscale methods can give us insight into the physics and chemistry of what is happening at the nanoscale, but there are cases when it is crucial to obtain true nanoscale resolution to make sound conclusions. The key methods for nanoscale imaging include the following: 1) electron microscopy (transmission and scanning approaches); 2) scanning probe microscopies (scanning tunneling microscopy (STM)^[15] and atomic force microscopy (AFM), [16] scanning near-field optical microscopy $(SNOM))_{s}^{[17]}$ 3) super-resolution microscopies [$^{[\bar{1}8,19]}$ such as stimulated emission depletion (STED), stochastic optical reconstruction microscopy (STORM), and less common approaches, which received well-deserved attention in cellular biology.

We expect that the basic principles of these methods to be familiar to the readers. The focus of this work is extracting properties beyond microscopy by AFM-based methods. They are particularly suitable for the device characterization and in recent decades have developed several modifications to access a range of material properties. Figure 1 shows the methods considered in this article classified by the properties characterized by them: electrical and (opto)electronic properties crucial for electrical contacts, local stress and strain that determine the N/MEMS performance, and the chemical composition of the materials focusing on coupling AFM with optical spectroscopy methods. The diagram shows that sometimes the same method can be used to obtain information about several characteristics: thus the basics of the methods are described in the section with the highest relevance. In the investigation of each material property, we will go from describing the most conventional ways for material analysis and proceed to the methods that enable the particular nanocharacterization, i.e., measurements with a nanoscale spatial resolution. Special attention will be given to the systems such as silicon nanosensors (N/MEMS) and CNTs studied by these advanced methods combining AFM with optical



Evgeniya Sheremet received her Ph.D. from Chemnitz University of Technology in Experimental Physics in 2015 for her thesis in "Micro- and nano-Raman characterization organic and inorganic materials." She continued her work on nanocharacterization including KPFM in the Solid Surfaces Analysis group of TU Chemnitz, and from 2017 became

a full Professor at Tomsk Polytechnic University, Russia. She continues her work in the field of nanospectroscopy and carbon materials and their applications.



Raul D. Rodriguez received a Ph.D. in Physics and Chemistry of Nanomaterials in 2009 with the highest honors at the Institut des NanoSciences de Paris, Pierre et Marie Curie University (Sorbonne Universités). In 2011, he joined the DFG Research Unit Sensoric Microand Nano-Systems in the Semiconductor Physics group at TU

Chemnitz, Germany. He developed and implemented novel methods for nanoscale characterization (TERS, CSAFM, KPFM, and nano-Vis). In 2017, he was appointed as full Professor at Tomsk Polytechnic University, Russia, focusing on novel plasmonic and 2D nanomaterials for technological developments including biomedicine, optoelectronics, energy, and safety applications.



Dietrich R. T. Zahn received his Ph.D. from the University of Wales. After doing post-doc at TU Berlin he became Professor for Semiconductor Physics at the Chemnitz University of Technology in 1993. His research focuses on the spectroscopic characterization of semiconductor surfaces, interfaces, ultra-thin films, low-dimensional structures. He served

as Pro-rector for Research and as Head of the Thin Film Division of the German Physical Society (DFG). He is Speaker of the DFG Research Units FOR 1154 "Towards Molecular Spintronics" and FOR 1713 "Sensorical Micro and Nano Systems", Vice President of the German Vacuum Society (DVG), and President of the Gaede Foundation.

excitation and/or detection. These material systems will best exemplify the benefits of such nanoscale characterization approaches.

2. Electrical Properties

Advanced characterization techniques for electrical and electronic properties such as a local conductivity and capacitance



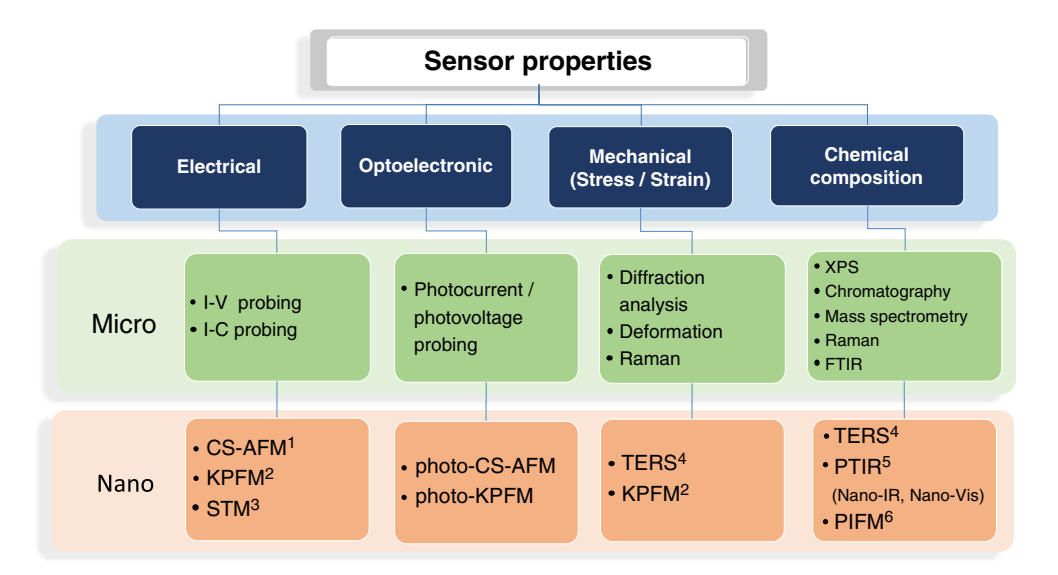


Figure 1. The methods considered in this feature article classified by the accessed property. The top methods (with green background) are used for macro- and microscale measurements, whereas those listed in the bottom (with orange background) are the nanoscale methods. ¹CS-AFM—current-sensing AFM. ²KPFM—Kelvin probe force microscopy. ³STM—scanning tunneling microscopy. ⁴TERS—tip-enhanced Raman spectroscopy. ⁵PTIR—Photothermal induced resonance. ⁶PIFM—photo-induced force microscopy.

are a fundamental prerequisite for reliability monitoring of all the electronic components and devices. Broadly taken, the topic can be differentiated into the following applications: 1) characterization techniques for increasingly miniaturized electrical and electronic devices following the trajectory of Moore's law from the micro- to the nanoscale using conventional current–voltage measurement equipment for molecular and other bottom-up devices,^[20] and top-down MOSFETs^[21] and 2) scanning-probe techniques such as conductive AFM,^[22] current-sensing AFM (CSAFM),^[23] and Kelvin probe force microscopy (KPFM)^[24] for material characterization.

2.1. Conventional Electrical Characterization

For the first of these two research paths, appropriate microprobes and approaches for the highest electrical as well as mechanical precision had to be developed in line with the trajectory of device miniaturization. Experiments for conventional electrical characterization of the micro- and nanoelectronic components are usually carried out on mechanical probe stations (hardware examples: FormFactor, Inseto, and Micromanipulator), equipped with a set of fast and high-precision source and measurement units (hardware examples: Keithley and Agilent). Similar to contemporary measurement technology, conductivity and capacitance are measured by applying an electric field to the sample and measuring its response using the respective electrodes. Wafer-scale elementary electronic nanocharacterization dates back to the early 2000s when, e.g., Berliocchi et al. [25,26] reported on scalable electrical characterization (static current-voltage characteristics) of CNT aggregates (bundles, tablets, ribbons, and films) between metal electrodes. They observed that the particular aggregation state of nanomaterials was decisive for the static electrical performance of the assembled nanodevice. The

sequence of the sample preparation, comprising 1) deposition of the carbon nanomaterials in a microstructured multi-finger structure from the liquid phase (e.g., droplet immersion); 2) dielectrophoretic alignment; and 3) various chemical treatments proved to alter the device performance significantly. To cope with occasional deviations and aging effects, experiments for different structural modifications were carried out under controlled environmental conditions (e.g., vacuum) and were performed repeatedly on different time scales (minutes, days, and weeks).^[26]

2.2. Nanoscale Mapping of Electronic Properties

As one of the many applications, we can take a closer look at CNT devices. Special cases of such are interconnects formed by vertically aligned CNTs grown by means of chemical vapor deposition (CVD), [23,27-30] mechanically bendable conductive lines made from conductive CNTs, [31] and horizontally aligned conductive tracks using multi-walled CNTs (MWCNTs) as well as CNTFETs using semiconducting SWCNTs.^[32,33] For the first case of CNT vias, local electrical probing allowed a resistivity mapping of grown CNTs or mapping down to the individual CNT. [23] For the second case of assemblies of MWCNTs, conductivity measurements using CS-AFM allow insight into the role of the local morphology represented by the preferential orientation on the nanoscale of the inkjet-printed lines on the microscopic conductivity. [31] For the third case of CNTFETs, the initial degree of positioning, [34] CNT assembly and alignment, contact formation [33] as well as the doping state [32] of the channel-building nanomaterial turned out to be important parameters. Particular challenges of hyperlocal electrical characterization are the variations of the environmental charge distribution both locally as well as temporally. They may be imposed





for instance by trap states in the gate dielectric varying the screening of the local electric field. The timescales range from microseconds to seconds. An evaluation of small signal data. noise characterization, fast data acquisition, and high-impedance sampling for single-nanotube devices (incompatible with standard 50Ω measurement equipment) proved to be a particular technical challenge for the electronic characterization. Furthermore, a particular consideration of dynamic probing based on pulsed voltage actuation turned out to be inevitable for proper nanoelectronic device characterization.^[35] Besides manual and automated microprobe stages, latest hardware developments for advanced nanoelectronic characterization include electrical contacts with high-precision microrobots or nanomanipulators (hardware examples: Imina, Kammrath & Weiss), enabling electrical measurements inside vacuum vessels for scanning electron microscopy (SEM) and other advanced characterization equipment (e.g., AFM and Raman setups) during the electrical device operation.

2.3. Scanning Probe Techniques I: STM and AFM

For the second path of scanning probe techniques, the nanoprobes required the development of unprecedented mechanical precision at maintained electrical precision. The main scanning probe techniques are AFM^[16] as well as the STM, ^[15] while there are plenty of advanced modes, particularly those recently developed for mechanical property testing [36,37] and for soft-matter and biomaterials. [38] Nanoscale conductance measurements based on STM serve as an ideal tool to study the relationships between structure and property on the atomic and molecular levels. STM and scanning tunneling spectroscopy were used to study the morphology of both SWCNT solids [39,40] as well as the interaction SWCNT solids functionalized with molecular moieties.^[41] An STM imaging with atomic resolution was used to resolve the noncovalent interaction between SWCNTs and pyrene as well as anthracene moieties by appropriate assignment of the molecular orbitals.^[42] For two decades up to date, differential conductance imaging has been used to perform nanoscopic imaging of interfaces of organic and molecular electronic materials, [43,44] topological insulators, [45] or, in particular, in nanomaterial heterojunctions, [46,47] even though this technique is primarily applicable only to conductive samples.

While STM allows a higher vertical resolution of the topography (picometer scale) when compared with AFM, it additionally shows the local density of states of the material surface probed. Furthermore, STM is limited to conductive samples. Nevertheless, it is a powerful technique in different fields like surface science allowing the electrical transport to be studied in different configurations as explained elsewhere. [48] In contrast, in AFM, the typical vertical resolution is on the order of 0.1 nm and the lateral resolution is mainly dependent on the tip diameter. Moreover, the high force sensitivity of AFM allows its application in the determination of other material properties beyond topography. For example, the reviews by Butt et al. [49] and by Garcia and Perez^[50] provide a comprehensive discussion of force spectroscopy in contact and dynamic AFM, respectively. For electrical measurements, silicon-based AFM probes are coated with a thin metal layer, typically a few nanometers to tens of nanometers, thus diminishing the spatial resolution at an increased tip diameter of around 50 nm. Alternatively, a conductive carbon/diamond layer can be applied to the tips, which may lead to local tip diameters of <20 nm due to the polycrystalline structure of diamond. [51,52] Compared with the metal layer, the diamond layer has superior properties: it is much harder and has

While there are many different types of measurement methods in AFM/STM and similar systems, [53] here we can focus on CS-AFM and KPFM. In general, it can be distinguished between current sensing and force sensing techniques; thus, CS-AFM belongs to the former and KPFM to the latter.

2.4. Scanning Probe Techniques II: Local Measurements of **Electrical Current**

In CS-AFM, the AFM is operated in contact mode. While simultaneously applying a constant voltage between the tip and the sample, the currents flowing between tip and sample are measured with a nanoscale spatial resolution. The lateral resolution is limited by the tip apex diameter, which is typically in the order of a few tens of nanometers. The electrical resolution is determined by the precision of the current-to-voltage amplifier. The latter is given by the thermal noise of the feedback resistor of the system and can be minimized by choosing a resistor value as large as possible. [54] A typical system on the market may have current sensitivities depending on the resistor values of the cantilever heads (also known as "nose cones"): $0.1 \, \text{nA} \, \text{V}^{-1}$ (for a nose cone with a $10 \,\mathrm{G}\Omega$ resistor), $1 \,\mathrm{nA} \,\mathrm{V}^{-1}$ ($1 \,\mathrm{G}\Omega$), or 10 nA V^{-1} (0.1 GΩ).^[55]

The nature of the challenges remains the same as in the macroscopic measurement techniques: controlling the current path, identifying parasitic resistances, and ensuring contact reproducibility. The tip apex shape, any contamination, or the wear-off of the metal coating due to the high strength of the electric field or mechanical damage can affect the measurement result. Due to the high pressure applied to both tip and sample in contact mode, this method can alter soft samples. A slightly modified version, though not implemented in all AFM systems on the market, is the jumping mode, where the tip is retracted to a certain height, while going from point to point, reducing the lateral forces. At each new measurement point, the tip is approached up to a certain force/setpoint in order to measure the current.^[53]

Initially, current-voltage mapping by CS-AFM^[28] was performed on CNT interconnect samples, for which resistivity changes can be governed by interface effects between the CNT and the metallization. An important nanostructured component in microelectronics is vertical interconnects made from carbon nanotubes (abbreviated CNT vias). They consist of vertically aligned conductive CNTs (mostly vertically aligned MWCNTs), obtained by CVD. CS-AFM applied to CNT vias allowed us to distinguish the effects of the single CNT quality and the contact quality. CNT vias connecting different metal levels of an integrated circuit are potential candidates to replace copper ones. With tip radii of the order of 20 nm, [56] the size ranges of the probe (metallized AFM tip) and sample (individual MWCNT) are comparable, the wafer-level fabrication process yields an appropriate mechanical stability and

www.pss-a.com

contaminations directly relate to the variation of the local conductivity properties (see below), therefore CNT vias appeared as ideal sample to verify the opportunities of CS-AFM as an advanced nanoscale characterization technique. The analysis of CNT via samples with CS-AFM reveals that different CNT vias yield a map of locally different conductivity as shown in **Figure 2** (left).^[23] The spatial resolution of about 40 nm suggests that the conductivity of a single MWCNT is accessible. Thus, the conductivity variations observed are those of individual MWCNTs.

For the variation of the conductivity of each MWCNT, there are two possible reasons: first, the CNT quality can scatter due to the on-chip growth—such that the intrinsic CNT conductance alters. In an earlier study, Teichert et al.^[57–59] could demonstrate the strong impact of the number of defects on the CNT conductance. Second, it is likely that the conductance of the CNT-metal contact can vary—as a function of contact material^[60,61] and processing.^[23] Thus, another method that discriminates these two contributions to the scattering of charge carriers, the first one intrinsic to the channel and the second one as a contact effect, is required.

Thus, to disentangle the difference between intrinsic conductance and contact effects, characterization techniques are able to answer the question of whether the CNT quality is homogeneous. Raman spectroscopy is the tool of choice for this task as it grants access to the defect density from the so-called D/G-intensity ratio: $^{[63-65]}$ the intensity ratio of the Raman D-line at 1351 cm⁻¹ (defect-activated Raman response of the imperfect sp²-lattice) and the Raman G-line at 1582 cm⁻¹ (Raman response of the sp²-lattice). This ratio is a qualitative measure of the defect density and thus a measure of the CNT quality and even of the nature of the defect.^[63–66] For the present study, a comparative Raman study of the different vias is required to discriminate the two degradation mechanisms: it becomes visible that the defect density within the CNTs is about the same, which results in the same intrinsic conductance. [23] Thus, the bottom contact of the CNT vias is expected to determine the performance. It is composed of the following layer system: Cu (substrate for electrical contact), TaN (20 nm, barrier against Cu diffusion), and Ta (10 nm, CNT-contact material; forms carbides at the CNT contacts). The diffusion of Cu is detrimental for CNT quality and must, therefore, be restricted. [67] After the CNT growth, the CNTs are embedded into SiO_2 using tetraethylorthosilicate (TEOS, $Si(O-C_2H_5)_4$) CVD, which has oxidizing properties. It is assumed that this procedure also oxidizes the tantalum, which degrades the contact. To characterize the atomic composition, transmission electron microscopy (TEM) investigations are required; the composition of the bottom material indeed shows the partial oxidation of the tantalum. [23]

As the TEOS CVD is required to embed and to protect the CNTs in SiO₂; the contact material must become more robust against oxidation. In a further study, it was shown that exchanging Ta with TiN, the conductance of the CNT vias became almost perfectly homogeneous while maintaining the CNT quality and homogeneity after the growth. This basically shows how CS-AFM, Raman investigations, and TEM can work together to optimize CNT growth in CNT vias or interconnect structures and to obtain a yield of 95%. An overall summary of the results of the consecutive process steps, which help to improve the contact resistance, is shown in Figure 2 (right). [23,56]

Based on the previous success with the TiN bottom layer, a more systematic study of the influence of the contact materials (bottom: Ta, TaN, and TiN, top: Ta, Ti, TiN) was performed. The best CNT vias are obtained using TiN for the bottom contact and Ta or Ti for the top contact while maintaining the yield. [68]

2.5. Scanning Probe Techniques III: KPFM

While CS-AFM determines the flowing current and STM uses the tunneling current to image surface atomic structure, KPFM detects an additional electric force that allows analyzing the surface potential of surfaces, [69,70] charge distribution, and diffusion in devices. [71] For metallic samples, the measured contact potential difference (CPD) between tip and sample allows

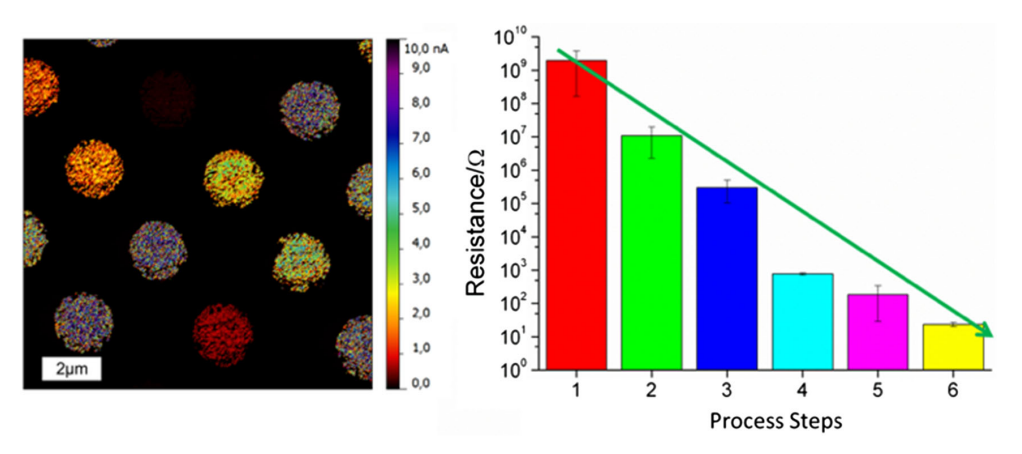


Figure 2. Left: CS-AFM image (top view) of an array of vertically aligned multi-walled CNTs (VA-MWCNT) integrated as vertical interconnects (diameter $\approx 2 \,\mu m$) after chemical–mechanical polishing in a copper damascene process, obtained at a bias voltage of 50 mV for a Cu-TaN-Ta bottom contact. Different colors belong to different local currents through several individual CNTs. Reproduced with permission. [62] Copyright 2011, The Authors, published by Fraunhofer ENAS. Right: Resistance of a series of VA-MWCNT vias at different process: steps 1) before thermal annealing (TA) and chemical–mechanical planarization (CMP); 2) after TA, no CMP; 3) after CMP, no TA; 4) after CMP and TA; 5) with improved top metallization; 6) with an improved bottom and top metallization. Figure created for this feature article is based on aggregated data and methods as described by Fiedler and coworkers. [10,15,48–50]

determining the work function of the sample based on the previous determination of the work function of the tip. For semiconducting samples, the CPD can visualize the Fermi-level position but also locally trapped charges can be observed using this method.^[72,73]

The principle is based on the interaction that takes place when two closely located surfaces are electrically contacted. In this case, an electrostatic force between tip and sample is generated. To detect the force, an AC voltage is applied to the tip, resulting in the force contributions appearing among others at the AC voltage frequency ω . In **Figure 3**, the external feedback loop attempts to nullify this force F_{ω} by applying an additional DC voltage which is equal to the CPD to the tip. The CPD is also sometimes referred to as the surface potential (SP), though it must always be seen in a reference to the tip's potential. Several KPFM modes can be distinguished, such as the lift mode versus the dualfrequency mode. In lift mode, the topography is acquired in the first pass in intermittent-contact mode. Afterwards, the tip is retracted at a distance between 5 and 100 nm, and the surface potential is determined by scanning the surface following the topography information recorded in the first pass. Another possibility is to obtain the topography and the electrical information within a single-pass using a different frequency for the AC voltage. This simultaneous measurement requires another lock-in amplifier. In general, a better lateral resolution is expected when the tip is closer to the sample, but the dual-frequency mode is more affected by polarization effects, and cross talk between topography and KPFM signal.^[75] Quantitatively, this means that the lateral resolution is in the range 20-50 nm for distances $d < 10 \,\mathrm{nm}$ between tip and sample in air, whereas in UHV the lateral resolution can be improved down to 10 nm.^[72] Regarding the electrical resolution, Jacobs reported a potential sensitivity in ranges lower than 1 mV for lift-mode experiments. However, care needs to be taken whether the absolute values of the surface potential are trustworthy and not dependent on distance. $^{[76]}$

For both of the aforementioned KPFM measurement approaches, the amplitude of the cantilever is determined and nullified, i.e., the electrostatic force is measured. This mode is being referred to as amplitude-modulated (AM-KPFM). In frequency-modulated KPFM (FM-KPFM) instead, the force gradient is nullified. This technique is based on the fact that the cantilever's resonance frequency $f_{\rm res}$ is affected by all long-range forces including electrostatic force. Thus, not only the frequency of the mechanical oscillation shifts, but also additional resonance modes of the cantilever appear at $f_{\rm res} \pm \omega/(2\pi)$ and $f_{\rm res} \pm \omega/\pi$. In FM-KPFM, the signal of the $f_{\rm res} \pm f_{\rm AC}$ is nullified by finding the correct bias voltage which equals $V_{\rm CPD}$. $^{[77]}$

Both modes, AM- as well as FM-KPFM, have their advantages and disadvantages: for example, Zerweck et al. and Glatzel et al.^[78] state that the KPFM signal depends on the tip geometry. The FM-KPFM is more accurate for objects smaller than the tip radius, whereas in AM-KPFM, the tip should have a similar size compared with the object measured. Furthermore, they believe that the signal is distance-dependent but this effect can be excluded for FM-KPFM within 30 nm distance of tip and sample. In FM-KPFM, the sensitivity is lower, requiring a higher AC voltage amplitude. This, however, may induce additional band bending, e.g., on semiconducting surfaces. In contrast to that, AM-KPFM requires only low AC voltages at a higher energy resolution, while averaging over the tip radius may cause the lateral resolution to be worse.

In general, using KPFM to determine the work function can allow optimizing even the sample properties according to specific requirements. As an example, Spadafora et al. studied metallic SWCNT networks on different substrates, for which they modified the metal nanoparticle functionalization to tune the work function. This handling allows improving the

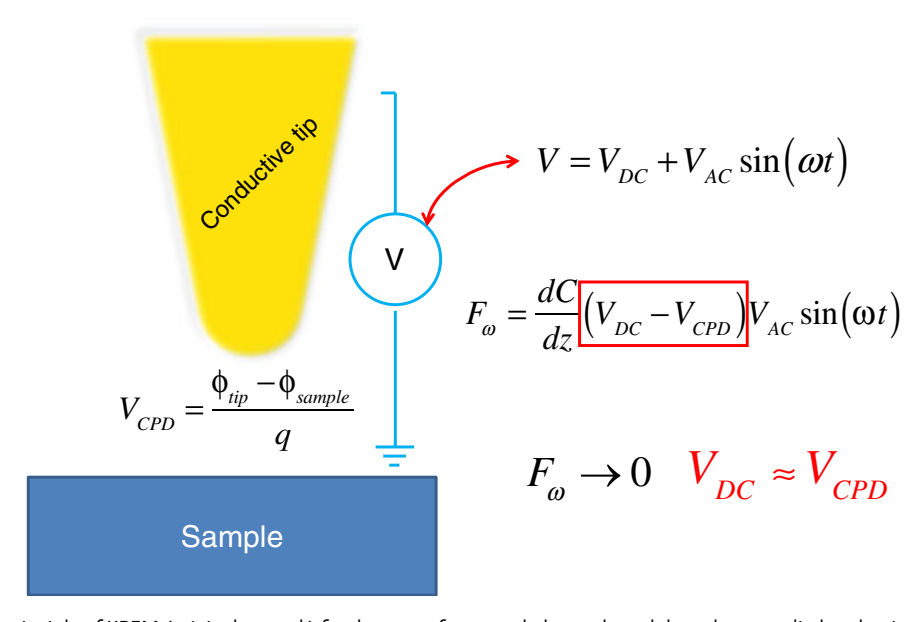


Figure 3. The working principle of KPFM (original artwork) for the case of a grounded sample and the voltage applied to the tip. A detailed description is given by Sadewasser and Glatzel.^[74]





contact properties when adding any additional interfacial active materials. $^{\left[79\right]}$

2.6. The Potential of KPFM and CS-AFM and Further Developments

The potential of CS-AFM for electrically conductive samples can be exemplified by the studies of CNT via structures, for which current–voltage characteristics were used to determine the resistivity. In conjunction with Raman spectroscopy as an optical characterization method, the CNT vias can be optimized in terms of performance and reproducibility.

For the KPFM method which measures the local surface potential difference between the tip and a conductive and semiconducting sample, two operating principles were introduced: AM-KPFM and FM-KPFM. The choice whether AM-KPFM or FM-KPFM is applied depends on the demands of the measurement: the higher lateral resolution of the FM-KPFM (a fraction of the tip radius) comes at the cost of a possibly reduced surface potential precision due to band bending for larger fields.

As a final consequence, the resolution of all described methods scales with the tip size: the sharper the tip, the better the local resolution and the signal amplification due to increased local fields, which is reflected by the vivid development ongoing in the field of tips and cantilevers.^[80–87]

3. Optoelectronic Properties

For optoelectronic sensors, characterizing and tuning the electronic properties is essential. But also, for any devices exposed to light-matter interaction such as solar cells or photodetectors, it is crucial to measure the effects of the incident light on the electronic properties of the device. This characterization requires the application of optical as well as electrical methods or their combination. The sensor relevant properties are absorbance and photoconductivity. As discussed in Section 1, CNTFETs are nanoelectronic devices that combine good current-carrying and well-understood switching properties with a small geometrical footprint in the order of 1 µm² and below. In CNTFET-based photodetectors, resonant optical excitation of one or a few CNTs generates either an electric current or, in the open-circuit configuration, a photovoltage which can be read out and processed further electronically. [88–90] The large surface-to-volume ratio makes the electronic and optoelectronic properties of SWCNTs especially sensitive to their environment. Thus, the smallest perturbations by external fields and their interaction with the CNT excited states can be used for tuning the physical and chemical properties of the transistor channel.^[90] These facts make CNTFETs ideal candidates for nanometer-sized, chemically sensitive light detectors and emitters. Using gold nanoparticles in combination with semiconductors is also another efficient approach to strongly increase the light/dark current ratio. [91] Such plasmonic-assisted improvement is part of our motivation to integrate gold nanoparticles in CNTFETs as discussed in Section 5.7.

3.1. Local Optical Properties: SNOM

Methods for a determination of the refractive index of materials below the diffraction limit as an optoelectronic property are often based on SNOM, also referred to near-field scanning optical microscopy (NSOM).[92] Bouhelier subsumes under the umbrella term SNOM "technique(s) capable of optically investigating the surface of a sample to form either a high-resolution 2D image or to perform local spectroscopy."^[93] In contrast to conventional optical microscopy, the lateral resolution attained with SNOM is typically much smaller than the wavelength and is mainly limited by the size of the optical probe used by the apparatus. Method classes comprise aperture-type SNOM^[94,95] and aperture-less SNOM. [92] Scattering-type SNOM (s-SNOM) has evolved as basis for local Fourier-transform infrared spectroscopy (nano-FTIR) to map the local dielectric constants of objects smaller than 200 nm with a resolution of 20 nm. [96,97] The genesis of these classes of analytics methods has also created tip-enhanced versions of SNOM^[98] or methods relying on the determination of optical forces occurring between the dipoles induced in the plasmonic tip and the sample under illumination. [99,100] Recent achievements comprise the combinations of SNOM with vibrational spectroscopy techniques correlating the spectra of a scattered optical near-field with molecular vibrational modes. [101] All these methods are also relevant for nanoscale chemical mapping (see Section 5).

3.2. Photocurrent Measurements: Mapping and Spectroscopy

Photocurrent mapping and photocurrent spectroscopy are two examples of optoelectronic characterization techniques^[102–104] that proved spatial resolution below 1 µm (cf. Figure 4c). These techniques were proposed as tools to study the local and spectral photoresponses, respectively, in situ. In contrast to CS-AFM discussed in the previous section, these photocurrent techniques do not comprise a scanning solid probe. Conversely, they use light in the visible or IR range to stimulate the microand nanoscale electronic devices in particular configurations. The photo-induced current (the drain current in case of transistors) is monitored as a function of the in-plane location of the incidence radiation and/or its wavelength. Meanwhile, commercial solutions for time-resolved photocurrent mapping are available measuring the temporal response of photo-sensitive materials to time-resolved illumination. Brick wall for these techniques, as for all scanning techniques, are the limits in time resolution on account of data integration which are typically a few 10 µs up to milliseconds per time interval at current noise levels in the order of 1 pA.^[105] Regarding the spatial resolution, Krupke and coworkers proposed a tip-enhanced photocurrent mapping exploiting plasmonically enhanced absorption induced by an optical nanoantenna and claimed a spatial resolution figure of 30 nm, measuring along a single SWCNT. [106] Figure 4a–c shows a principle sketch of a further method proposed by Krupke and coworkers using a combined photocurrent mapping and photocurrent spectroscopy. Herein, both the current noise level and the spatial resolution are slightly worse, but the combination of microscopy and spectroscopy allows to determining the distribution of particular CNT chiralities inside the transistor channel

www nss-a com

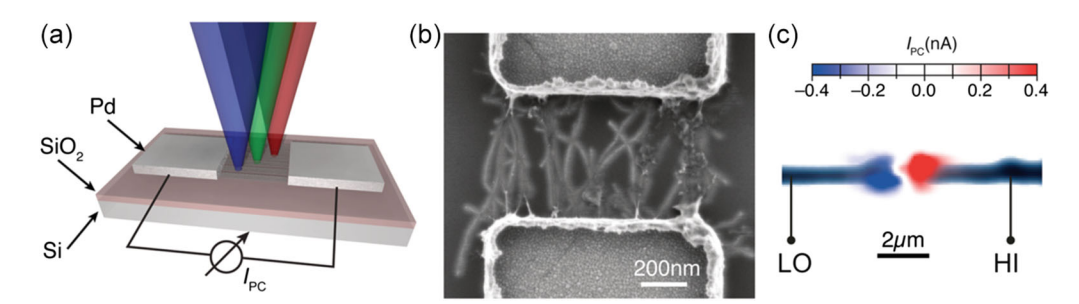


Figure 4. a) A 3D schematic view of the measurement setup for spectrally resolved photocurrent mapping on a component of a device consisting of CNTs of various chiralities. A focused light beam of variable wavelength is scanned across a film or network of aligned CNTs which is interfaced with metallic contacts. b) Scanning electron micrograph of a typical CNT device as schematically shown in a), where the CNT density is approximately 10 µm⁻¹. c) Scanning photocurrent microscopy map (excited at 570 nm) overlaid on top of the simultaneously recorded elastically scattered signal from the sample. Reproduced with permission.[103] Copyright 2014, American Chemical Society.

of a working optoelectronic device fabricated from solutionprocessed SWCNTs.[103] Holleitner and coworkers proposed ultrafast time-resolved photocurrent spectroscopy to probe exciton dissociation and ballistic transport in 1D materials in a transistor channel.[107]

Photocurrent spectroscopy was also applied to the detection of bright and dark exciton transitions in 2D materials such as MoSe₂.^[108] Herein, bright excitons are optically active whereas dark excitons are per se spin forbidden. Quereda et al. also put forward a concept for the integration of electrically driven photoemissive CNTs and coupling their light into waveguides^[109,110] and quantum photonic circuits.^[111] Hybrid entities made from stacked sequences of 2D materials (graphene, layered transition-metal dichalcogenides) were proposed as components for high-fidelity sensor systems. [112]

3.3. Local Photoelectronic Properties: KPFM under Illumination

KPFM is an AFM-based method that allows the measurement of the CPD between the tip and the sample. [113] The working principle is based on minimizing the electrostatic force between the tip and the sample that occurs due to surface potential difference (cf. also Section 2.3). Performing such measurements under illumination gives insight into the local photoelectronic properties.

This set of methods can be used to determine Fermi-level shifts under illumination. Recently, photoassisted KPFM was reported as an innovative method to detect the doping type in GaN nanowires correlating with the CPD detected under illumination with super-bandgap light in photoassisted KPFM. The results were explained by electrons generated in the *n*-type region under illumination. These electrons were supposed to be withdrawn from the surface and the holes to be attracted to it by the electric fields in the space-charge region. [114] Especially in the field of solar energy harvesting, KPFM measurements under illumination and in darkness became a well-established technique for the tracing of structure-property relationships in the active photovoltaic materials. Herein, the local surface photovoltage (SPV) is measured as the change in CPD between the KPFM tip and the sample surface upon optical illumination. Shortpulsed illumination gave direct access to the difference in the CPD between illuminated and dark states and hence relate back to the particular decay times of the SPV and/or its wavelength dependence. [115] Herein, Figure 5 shows the respective setup, a block diagram, and a measurement scheme for the timedomain KPFM measurements. Mapping of the surface potential using KPFM was also used in multiferroic BiFeO₃ nanowires (BFO-NWs) under sub-bandgap illumination.[115]

The mechanism of photovoltage generation in BFO-NWs was detected by local illumination of visible laser pulses at different positions of the BFO-NWs and mapping of the photoresponse.[116] Already a decade ago, Sadewasser et al. proposed KPFM as a technique to probe the optoelectronic effect of Zn doping in polycrystalline CuInS2 thin films implementing a local surface photovoltage spectroscopy (SPS). SPS was measured using KPFM to obtain the SPV and SPS with a high lateral resolution, correlating to the homogeneity of the doping in the films.[117]

3.4. New Trends in Optoelectronic Devices and Their Nanocharacterization

Summarizing this section, an advanced nanoscale optoelectronic characterization is necessary for emerging device concepts especially from low-dimensional (1D, 2D) pure, hybrid, and nanoconjugate materials with tailored sensing properties. [118] From the current research, the beneficial sensoric add-ons comprise, e.g., the spectrally defined optical properties of the active sensing material through photo-induced electron transfer (PIET)[119] or scattering, [120] their chemical specificity at highest sensitivity, [121] and custom-oriented fabrication. [122–124] For optoelectronic sensors, grafting of 1D (nanotubes, nanowires) or 2D (graphene, MoS₂) nanomaterials with metal and metal oxide nanoparticles or colloidal semiconductor quantum dots was found to enhance the absorption of carbon-based materials and to enable high gains. [112] CNTFETs in combination with plasmonic nanoantennas were seen as a viable solution for the enhanced, optical sensor devices. [125] Beyond that, nanoconjugates (or hybrids) between CNTs and chromophoric or plasmonically active coaggregates can be seen as a recent scientific and technological trend. Consideration for sensor applications here is a tunability within a single class of materials: for a number of coaggregates, for instance, absorption, photoluminescence, or plasmonic



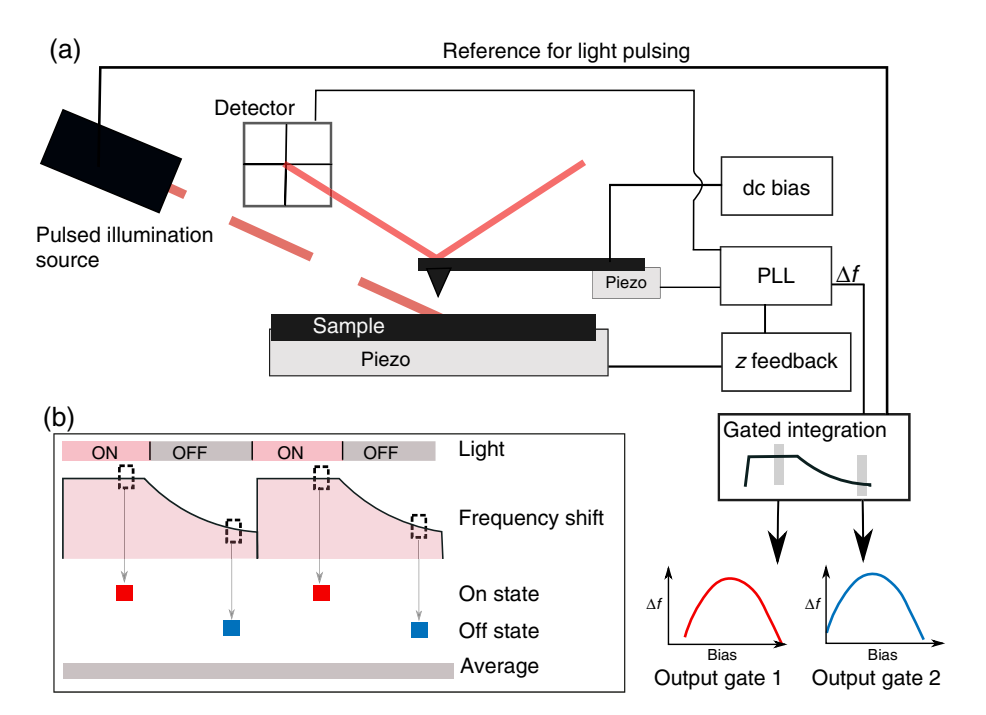


Figure 5. a) A setup and block diagram of the time-domain KPFM measurement. The frequency-shift signal is integrated with two gated integrations synchronized with the pulsed illumination. Each output of the gated integration is recorded at each applied bias to record a full Kelvin parabola. b) Measurement scheme for a gated integration in the time domain of the modulated frequency shift. Reproduced with permission. [115] Copyright 2016, American Physical Society.

properties can be tuned simply by the size and/or shape (CdSe/ZnS quantum dots, $^{[126-129]}$ metal nanoparticles, $^{[130,131]}$ and InP/ZnS nanoparticles^[132]). They can also be dependent on the polarization of the incident light (semiconductor quantum dots). [133-135] Regarding sensitivity, using CNT devices with gold nanoparticles, Mahjouri-Samani reported by far the highest sensor magnitudes (responsivity 800 VW⁻¹ instead of 70 VW⁻¹) and faster response times (25 ms instead of 100 ms) with plasmonically grafted CNTs. [125] The authors explained this behavior by the coupling of the laser beam into the surface of the metallic structures that, in turn, induces fast oscillations of the freeelectron system known as surface plasmon polaritons (SPPs). The energetic interactions are localized on a sub-wavelength scale at the tips of the plasmonic structures and, for the chosen ideal device geometry, couple efficiently into the CNTs due to strong electron-phonon interaction. Although the combination of optoplasmonic and optoelectronic transducers at the nanoscale has their perspectives, the limitations of this approach are the lack of standardized methods in the device systems integration at the micro-nano interface. Nanocharacterization for these classes of sensor devices requires advancement at the interface between optical techniques, scanning probe techniques, and electrical measurements with submicron resolution (cf. Section 2). A particular merging of techniques has taken place already in organic photovoltaics. Herein, the combination of nanoscale CS-AFM and intensity-modulated photocurrent spectroscopy (IMPS) has been mastered. Kumar et al. applied this analysis to interfaces in bulk-heterojunction (BHJ) solar cells. As a result, the nanoscale topography and the CS-AFM results indicated differences in the segregation state of the active

layer and the interfaces to the electrodes before and after certain annealing steps of the fabrication route. [136] Therefore, to render the endowments suitable for more commercial solutions, further efforts on aspects of device and system integration are required in the engineering sciences.

4. Micro- and Nanomechanical Stress and Strain Measurements

This section focuses on stress and strain determination on a micro- and nanoscopic spatial scale aiming to provide an overview of the applicable methods and lower boundaries in spatial resolution and sensitivity reported so far.

The need for characterization of stress (a physical quantity that aggregates the internal forces per area between infinitesimal constituents of a material, unit Pa) and strain (as the relative deformation of N/MEMS components, dimensionless) on a microand nanoscopic scale is manifold. The recent examples of application scenarios include, but are not limited to the determination of stress and strain for material characterization, [137,138] calibration of evaluation algorithms of MEMS sensors, [139] or the measurement of stress and strain in integrated circuits during or after fabrication.[140-142] While moving forward in miniaturization, stress and strain characterization on the true nanoscopic spatial scale becomes important to understand the properties and the behavior of potentially new materials and their interfaces; e.g., in the case of CNTs, it is known that the embedding itself affects the mechanical behavior of their interfaces. [143] After a successful understanding and integration of nanodevices,





the scenarios already mentioned become additionally significant again. Therefore, the tools have to be prepared.

By the scenarios already mentioned become additionally significant given as 10^{-3} . [15] be used on 1D or 10^{-3} .

While strain can be measured, stress is usually not measured directly. The determination of stress in a sample depends on the measurement of physical quantities such as displacements or potentials, and a physical model is needed to determine stress based on the strain. In addition, for the determination of stress, additional and often material-specific parameters as stress-free lattice spacings, elastic constants, or the positions of reference peaks are required. [140,144] The strain determination on a spatial micro- and nanoscopic scale is possible by a variety of techniques as for example X-ray diffraction (XRD) in many variations, electron backscatter diffraction (EBSD), low-energy electron diffraction (LEED), convergent beam electron diffraction (CBED), Raman spectroscopy, KPFM, or Focused Ion Beam-based Deformation Analysis by Correlation (fibDAC). However, all of these methods have limits especially with respect to the achievable spatial resolution.

4.1. Diffraction Methods

For diffraction methods, an incident beam on a sample is scattered at the crystal lattice and constructive interference creates a projection of the reciprocal lattice, which can be detected as a characteristic pattern called Kikuchi lines or Laue circles. The patterns can be analyzed to obtain strain and stress states within the sample by analyzing the change of the patterns in comparison with stress-free references.

The techniques of XRD and electron diffraction qualify for microdiffraction analysis. These methods may be applied for evaluating crystalline materials and thin films^[145,146] but not for monolayer structures like graphene or 1D materials as CNTs, as these samples do not provide the lattice structure needed to apply the methods.

The XRD methods are described as follows: High-resolution XRD (HR-XRD) $^{[147]}$ enables local stress analysis of single crystals and epitaxial films. For the local analysis of single and polycrystals, usually, microscanning XRD ($\mu SXRD)^{[148]}$ is used at synchrotron beamlines. The Kossel diffraction (electron-beam excitation) $^{[149]}$ and Pseudo-Kossel diffraction (synchrotron excitation) allow strain determination in the order of $10^{-6}.^{[150]}$ The XRD methods collect information distributed over an interaction volume of some $10\,\mu m^3$ and have usually high accuracy for out-of-plane components and lower accuracy for in-plane components. $^{[151]}$

Electron diffraction (ED) requires more or less extensive sample preparation. EBSD, typically available in SEM, can be used for cross-correlation of electron diffraction Kikuchi patterns from the sample under the unstressed and stressed conditions to determine strain in the stressed location. [144,152] CBED at the TEM (CBED) analyzes high-order Laue zone lines that are narrow ring lines away from the center of the diffraction pattern. Electrons show greater interaction with matter than X-rays providing surface-sensitive information with an interaction volume of some 100 nm^3 . The strain can be determined in the order of 10^{-4} – 10^{-3} . [153,154] LEED uses electrons with energies well below 1 KeV and its diffraction patterns contain therefore only surface information. [155] The order of determined strain in thin layers is

given as 10^{-3} . ^[156] In general, diffraction methods can only hardly be used on 1D objects such as CNTs or other nanomaterials, as they do not provide sufficient lattice volume needed to generate diffraction patterns.

4.2. Deformation Methods

Deformation analysis by correlation (DAC) and stress relief methods, the later one referenced as crack-compliance or slitting methods as well, are widely known macroscopic approaches which can be applied to the micro- and nanoscopic scale. Typically, these methods are used in the characterization of residual stresses in wafer compounds and possibly stacked structures on MEMS and even NEMS scale.

Focused Ion Beam-based DAC (fibDAC) [147,157,158] measures stress relief using digital image correlation after a Focused Ion Beam (FIB) milled a trench into a structure. The measured displacement patterns have to be compared in an additional step with analytically or numerically calculated displacement fields to identify the unknown values. [147] The method is applicable to a wide range of materials, can analyze multilayered structures, and does not presuppose any knowledge on the kind of stress analyzed. The spatial resolution of the fibDAC approach is given in the nanometer range according to the study. [158] fibDAC provides high accuracy for in-plane stress components of $\Delta\sigma=\pm70~\mathrm{MPa}^{[157]}$ but lower accuracy for out-of-plane stress components. [157]

The integration of appropriately designed test devices in the layout of a MEMS reticle offers a highly sensitive approach to determine residual tensile or compressive stresses in different layers of a given system of different materials. The bending, displacement, or rotation of the test devices is measured optically or by SEM and correlated to analytical or numerical models to characterize the stress distribution in the layers of interest. The stated detectable stress variations are typically smaller when compared with 20 MPa, [161,162] but for optimized devices even as small as 1.5 MPa.

4.3. Raman Spectroscopy

Raman spectroscopy $^{[163]}$ is a vibrational spectroscopy, where the sample is illuminated by monochromatic light, which is scattered inelastically due to excitation/relaxation of vibrations. This scattered light can be analyzed by an optical spectrometer. $^{[140]}$

The analysis of the position changes of Raman peaks allows determining stress and strain in a sample based on the detection of peak shifts in the Raman spectrum as the lattice vibrational frequency depends on the spacing between atoms. Therefore, the method can be used for a variety of Raman active materials as silicon, germanium, CNTs, and a range of other compounds. The position of the material-dependent peaks is not only stress dependent, but can be altered by temperature changes as well. To exclude such effects, typically two sets of spectra are recorded: a relaxed reference and the stressed state of the sample under investigation. By comparing both states, thermal influences caused by the laser can be identified and removed. [164] To increase the accuracy of Raman spectroscopy, external light sources such as Xe lamps or laser plasma lines are used as their

positions do not shift under stress or temperature changes of the sample. Only disturbances inside the Raman spectrometer such as mechanical shift, external vibrations, or thermal drift of the spectrometer grating, the mirrors, or in the optical table can shift the plasma peak. These shifts additionally and simultaneously influence the peak position from the sample and can, therefore, be used to compensate for potential external effects and instrumental artifacts such as thermal drift.^[164]

Raman spectroscopy does not require any complicated sample preparation and yields depth information depending on the optical absorption of the sample for the laser excitation wavelength. The spatial resolution depends on the wavelength and the numerical aperture (N.A.) of the objective lens; it can usually be considered below $2\,\mu\text{m}^2$. Considering silicon-based N/MEMS systems, the calculation of stress based on measured peak shifts depends strongly on the geometrical orientation of the sample and the stress patterns on the wafer. $^{[165,166]}$ In the case of uniaxial stress along the [110]-direction of the Si wafer, the following equation holds

$$\sigma_{\rm b}[{\rm MPa}] = -434 \times \Delta\omega[{\rm cm}^{-1}] \tag{1}$$

In this notation, σ_b represents the stress in the sample and $\Delta\omega$ describes the shift of the Raman frequency ω from its unloaded reference. The scaling factor -434 depends on several parameters like e.g., the phonon deformation potentials, for which several values are reported in the study. As of this, even the scaling factor may vary. The documented stress sensitivity is below 20 MPa even for geometrically challenging MEMS structures, whereas a limit of 10 MPa $^{[164,169]}$ is given in the study (Figure 6).

To reach high sensitivities below 20 MPa, not only highly sensitive equipment is needed, but also sophisticated post-processing of the acquired data is necessary as described in our earlier study.^[139] Instead of averaging among spectra to smoothen the data, every spectrum is analyzed and appropriate functions are fitted to the peaks of interest, e.g., Si and plasma

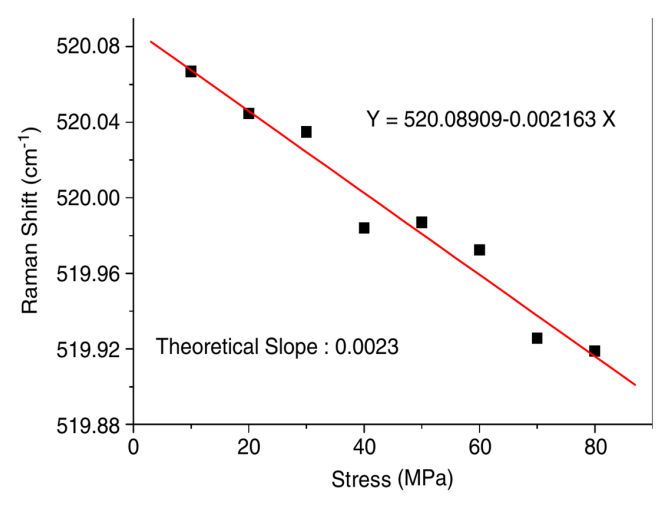


Figure 6. Results of a Raman spectroscopy measurement of a bent single-crystal silicon cantilever. Reproduced with permission.^[170] Copyright 2006, Elsevier Ltd.

peaks. Only if the fits comply with defined quality standards, the spectrum in question is considered further.

However, Raman spectroscopy provides a nanometer resolution only in tip-enhanced Raman spectroscopy (TERS) configuration by applying a plasmonic nanoantenna that localizes and enhances the electric field, as explained in more detail in Section 5.6. Using an AFM tip with a metal coating acting as a plasmonic nanoantenna, the TERS principle was used to map strain in CNTs, [171] MoS₂, [172] graphene, [173] and in Si/Ge quantum dots. [173,174]

4.4. Kelvin Probe Force Microscopy

KPFM^[70] (cf. Section 2.3) is a well-known variant of the AFM and among others can be used to analyze the work function of surfaces or, in other words, the surface potential. [69,70] However, the surface potential cannot be extracted directly, but merely a CPD. The measured CPD represents the difference between the work functions of the tip in use and the studied surface. Based on the knowledge of the work function of the tip, which can be obtained using a well-known reference sample, e.g. a gold layer of sufficient thickness, the work function of the sample can be calculated. The relation between change in surface potential and stress is reported to be linear with a scaling factor heavily depending on the studied material. The study states a limit of 1 kPa in stress sensitivity and successful applications of this method for the characterization of semiconducting silicon and metallic membranes.^[175] Figures 7 and 8 display initial setup and result of the Si-based experiment presented by Unal et al., [175] the pioneering publication for stress determination using KPFM: A Si-cantilever is bent by a bimorph and the CPD is measured by KPFM in the region with the highest expected stress. The CPD is correlated to numerically computed stress values using the generated displacement z.

Stress and strain characterization using KPFM has not yet become a standard technique. It is known that the CVD deposition of graphene intrinsically yields stress. [176] It was observed by KPFM and Raman that suspended areas of graphene flakes show greater stress and strain when compared with the supported areas proven by changes in the CPD and by correlating the G and 2D modes, respectively. [176] As a result of this, such properties of the deposition techniques need to be taken into account

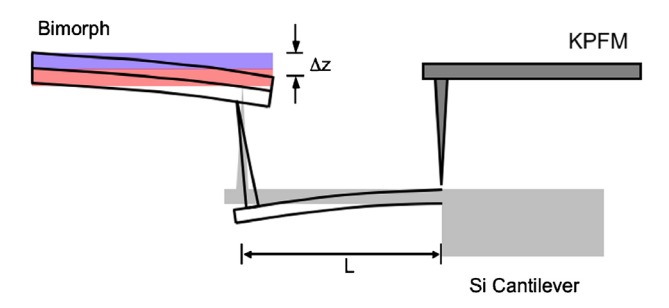


Figure 7. Experimental setup described by Unal et al.^[175] to induce and characterize stress in a Si cantilever using KPFM. The cantilever of length L is bent by a bimorph. The generated displacement (Δz) induces stress in the cantilever. Reproduced with permission.^[175] Copyright 2007, AIP Publishing.

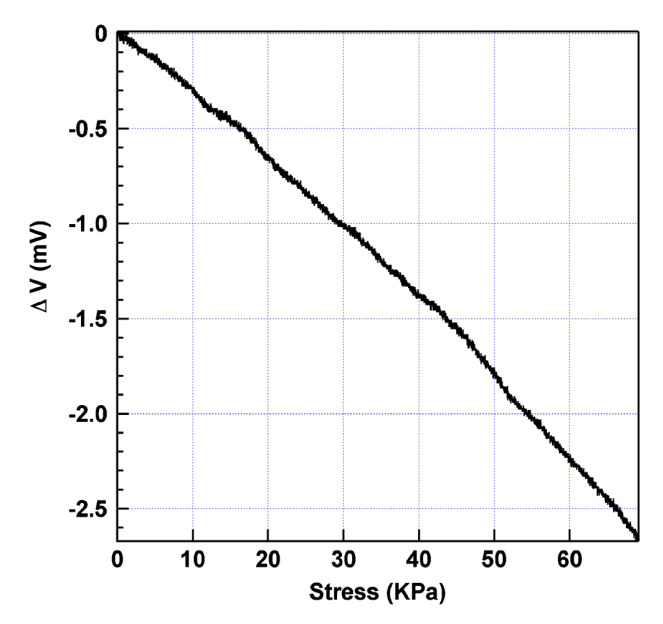


Figure 8. CPD at the base of a bent Si cantilever as a function of stress. Reproduced with permission. [175] Copyright 2007, AIP Publishing.

during device engineering and KPFM can be considered as one of the new trends in stress and strain measurements.

4.5. New Trends in Stress and Strain Measurements

The methods for stress and strain characterization discussed in this section qualify for an application even on a micro- or nanoscopic spatial scale. High sensitivity stress and strain measurements can be considered as a key to further miniaturization as the knowledge resulting from such measurements enables an understanding of materials and therefore reliable devices.

For the analysis of volumetric samples as crystalline materials and thin films, diffraction methods enable the user to perform high-precision measurements even on very small volumes. Integrating well-designed test samples using the deformation concepts into a fabrication process or analyzing a sample using fibDAC allows for precise monitoring of the stresses and strains in a general way. Initially applied to Si structures, Raman spectroscopy has become a versatile tool on the microscopic spatial scale and is currently pushed into the nanoscopic scale using the advanced TERS enhancements on new materials.

Stress and strain characterization using KPFM promises very high sensitivity. Currently, the study base for this method is limited, but the authors hope for the further developments on this promising approach.

5. Chemical Composition and Material Quality

Chemical composition is the most basic property determining the performance of any sensor. Its analysis is necessary to confirm the presence of a particular compound, identify contaminants, or verify the defect concentration. AFM is extremely limited in the chemical composition analysis and can only distinguish the phase contrast or mechanical properties of two materials. [177,178] It is only recently that it became possible to obtain a true nanoscale resolution of these properties versus the elemental composition that is long established in electron microscopy-based methods. The classical methods of chemical analysis include chromatography, mass spectrometry, X-ray photoelectron spectroscopy (XPS), and vibrational spectroscopy methods. The recent trends comprise nanospectroscopic methods (TERS, nano-IR, and PIFM) and combinations of two or more methods, touching even topics like in operando spectroscopies that shed light into structure analysis during catalytic activity. [179]

5.1. Chromatographic Methods

In general, in chromatographic systems, there are two phases, such as mobile phase and stationary phase, but those two phases must be immiscible. The mobile phase can be gas or liquid, whereas the stationary phase can be solid or liquid. According to the mobile phase, the chromatography is classified into two types: gas chromatography (GC)[180] and liquid chromatography (LC). [181] In operation, the chromatography system pumps a solvent to the analyzed samples, and the solvent dissolves the samples. The obtained solution ("mobile phase") passes through a separator column filled with a stationary phase. There the different constituents dissolved from the samples are separated relatively due to different masses, chemical affinities, polarities, etc. that will determine their different mobile speeds. Subsequently, the separated compositions of those constituents are determined by a specialized detector at a different time. From the detected signal, we can get the chromatogram. The peak intensity or area shows the content ratio of different compositions. This method is not suitable for spatially resolved imaging.

5.2. Mass Spectrometry

Mass spectrometry works based on the mass-to-charge ratio of ions. Therefore, an ionizing process is needed. There are several ion sources which can achieve this process, e.g., electrospray ionization (ESI),[182] fast atom bombardment (FAB),[183] chemical ionization (CI), [184] matrix-assisted laser desorption/ionization (MALDI),[185] etc. After ionization, different types of ions are formed. Those different types of ions with different massto-charge ratio pass a magnetic field. As they have different masses, the accelerations by the magnetic field are different and they are separated accordingly. Those separated ions finally come to a detector. Due to different speeds of those ions, they arrive at the detector at a different time or at different positions. Based on the positions or time they arrive, the mass-to-charge ratio can be determined and recorded, resulting in mass spectra, whereas the quantitative characteristics of those ions can be defined by the peak intensity or area. With those different mass-to-charge ratios, it is possible to analyze the components of the samples. By changing the desorption ionization technique, imaging of spatially resolved structures is possible. MALDI with different focusing approaches enables the focusing down to $5\,\mu m,$ or down to cellular levels. $^{[186-188]}$



5.3. X-Ray Photoelectron Spectroscopy

XPS is both a quantitative and qualitative analytical technique. The core principle of XPS is based on the photoelectric effect. When an X-ray with certain photon energy ($E_{\rm p}$) irradiates the surface of samples, and as the $E_{\rm p}$ is bigger than the electron binding energy ($E_{\rm b}$), the photons excite electrons in different orbitals, resulting in their ejection from the atoms with kinetic energy ($E_{\rm k}$). $E_{\rm k}$ can be measured by the detector of the XPS system. Thus, we have the function below

$$E_{\rm b} = E_{\rm p} - E_{\rm k} - \phi \tag{2}$$

φ is the work function, and it depends on the spectrometer. According to this equation, we can determine E_b . A given chemical bond has its own certain E_b , e.g. E_b of a C1s electron of a carbon atom in C—C bonding configuration is 284.5 eV, whereas E_b in C—O bond is 286.5 eV. ^[189,190] With the advancement in the X-ray optics, modern XPS setups can achieve resolutions of 3 μm (such as ESCALAB).

5.4. Vibrational Spectroscopies: FTIR and Raman

The measurements of the vibrational frequencies in materials allow characterizing not only chemical composition and structure but also strain (cf. Section 4.3), doping, defect concentration, $^{[191]}$ and the size of nanostructures. $^{[192]}$ The optical methods (FTIR and Raman spectroscopy) give so-called vibrational spectra, but their spatial resolution is fundamentally limited by the diffraction limit of light. They are known for their chemical specificity and are applied in many areas of science. An FTIR directly measures the IR light absorption at a specific frequency. Each absorption band corresponds to a vibrational frequency that is in turn determined by the mass of the atoms and the strength of the chemical bonds between them. A typical FTIR spectroscopy setup uses a millimeter-scale light spot but in microspectrometers equipped with objectives microscale resolution on the order of 10 μm has been achieved. $^{[193,194]}$

Unlike FTIR, Raman spectroscopy measures the loss (or gain) of the scattered photon energy with respect to the incident laser energy. The difference equals the vibrational frequency. Due to the different processes involved, FTIR and Raman spectroscopy signals follow different selection rules providing complementary information. The resolution in a microscopic configuration in Raman spectroscopy is determined by the diffraction limit described by Abbe's formula^[195]

$$\Delta x = 0.61\lambda/\text{N.A.} \tag{3}$$

Therefore, the resolution depends on the wavelength (λ) of incident light and the numerical aperture (N.A.) of the objective. The resolution values achieved are $\approx 1\,\mu\text{m}^{[194]}$ and can be as low as 0.3 μ m. However, recent developments allowed improving the spatial resolution of Raman spectroscopy beyond this limit using the solid immersion lenses, superlenses, superlenses, photon statistics, where time-multiplexing approaches, digital holographic super-resolved microscopy, etc.

5.5. Optical Absorption at the Nanoscale: PTIR (Nano-Vis, Nano-IR) and PIFM

The performance of the optical sensors and other optoelectronic devices is strongly influenced by their optical properties, and above all light absorption. Thus, this property is not only highly relevant to characterize devices, but also to investigate their chemical composition or quality. The optical properties on larger size scales are typically determined from the UV–vis or ellipsometric measurements, with their spatial resolution limited by diffraction. The analytic methods combining AFM with optical illumination have proven to beat the diffraction limit reaching a lateral resolution of the order of 10 nm and even sub-nanometer resolution. [203] Apart from s-SNOM (cf. Section 3.1) and TERS (cf. Section 5.6), PTIR microscopy. [204] was created as a technique to allow a nano(photo) chemical detection of samples. [101,205]

Optical absorption at the nanoscale can be measured and mapped indirectly using the photothermal expansion that a material experiences after illumination and light absorption. The detection of the tiny photothermal expansion, estimated for a particular example to be in the range of \approx 3 pm, [206] and its 2D mapping are possible by the amplification and detection capabilities of AFM cantilevers.^[207,208] When the laser source is spectrally tuned to the wavelength corresponding to absorption, there is a rapid thermal expansion of the absorbing part of the sample. In other words, thermal expansion occurs due to the vibrational motions of the molecule, which occur due to the absorption of infrared radiation, return to their original vibrational state. Thus, a tunable, pulsed laser is required, allowing the excitation wavelength to be changed to record the absorption spectrum. Each laser pulse causes thermal expansion, which in turn causes a force pulse at the AFM tip. Because of this, the cantilever oscillates, and the amplitude is proportional to the absorption of the sample. In the case of IR radiation, nano-IR can be performed giving detailed information about the material quality and chemical composition. If visible light is used, it is referred to as nano-Vis (cf. Figure 9), while the umbrella term is PTIR. [205,209,210] Closely related, using the same excitation scheme but modified probes, scanning thermal microscopy (SThM) reveals the local temperature of the sample. Since it does not extract any optical properties from that, we refer to a review article by Chapuis. [211] Even if photothermal microspectroscopy (PTMS), which belongs to SThM, allows an IR spectrum to be extracted, care needs to be taken not to mix it with the similar-seeming methods such as PTIR. PTMS requires sophisticated probes, originally Wollaston thermal probes, for temperature sensing; thus, the measurement method itself and its implementation are quite different.[212,213]

The most typical configuration for nano-IR is a thin film on an IR transparent ZnSe prism, which is illuminated from the bottom, [208] though top-side illumination allows the investigation of opaque samples. [207]

The use of an AFM tip allows measurements of absorption below the diffraction limit. $^{[208]}$ The measurement is difficult when the size of the object is less than 100 nm in height, thus an increased sensitivity of AFM-IR is obtained using the wavelet transform method (WT) for a 15 nm thick polymer

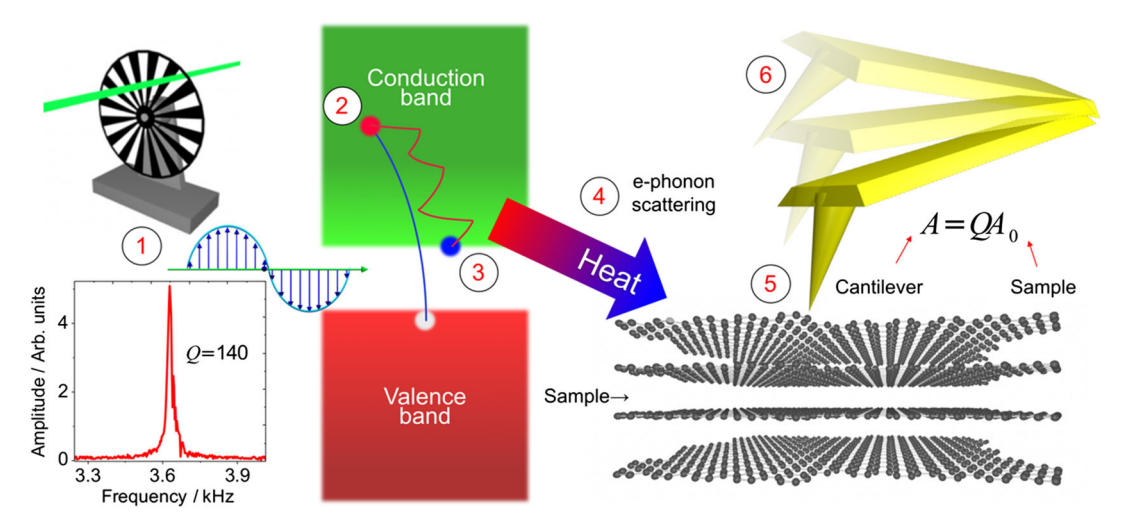


Figure 9. A schematic of nano-Vis. 1) Chopper wheel to create a pulsed laser beam and resonance spectrum of the cantilever. 2) The laser light is absorbed by inducing an electronic interband transition to the conduction band. 3) The excited electron relaxes to the bottom of the conduction band through e-phonon scattering resulting in heat 4) which induces 5) the thermal expansion of the sample (A_0). This thermal expansion is amplified (times Q) and detected by the cantilever 6) allowing the optical absorption event at the nanoscale to be tracked. For nano-IR and PTIR, the sample's photothermal expansion detection is very similar but a pulsed laser is used instead of a chopper wheel. Adapted with permission. Copyright 2018, American Chemical Society.

nanostructure. $^{[214]}$ The results on samples that contain the photosynthetic pigment-protein complex LHCII (light-harvesting complex II) showed a resolution of 20 nm. [215] This can be explained by the high absorption of IR radiation, the mechanical properties, and the thermal conductivity of proteins. However, the laser does not necessarily need to be pulsed at high frequencies, as our earlier study shows. [207] Herein, we utilized nano-Vis to demonstrate a spatial resolution of 4 nm using a chopper to modulate the laser at the resonance frequency of the cantilever. It is noted that nano-Vis is the only method of this kind that uses a mechanical chopper to modulate the optical excitation, although this modulation can also be achieved with a pulsed laser where the pulse frequency is externally controlled. However, implementation with a mechanical chopper allows using inexpensive laser diodes as light sources in nano-Vis. Moreover, by having a battery of laser diodes at different wavelengths, one can access the whole UV-Vis-NIR spectral range. Such versatility makes nano-Vis possible in any optically accessible AFM at a fraction of the cost of conventional PTIR and

A noncontact variation of nanoscale spectral recording is photo-induced force microscopy (PIFM). [216–218,205] It uses AFM to measure the dipole–dipole force gradients occurring between the sample and the metalized tip as wavelength-dependent polarization and transform them into an absorption spectrum resolving molecular vibrational resonances. [101] As the near-field interactions are also detected by the AFM tip, high spatial resolution below 10 nm was demonstrated, [99] allowing individual gold nanoparticles to be detected. [219] Using a tunable light source, it is also possible to recover the IR absorption spectra of the sample at the nanoscale. According to Murdick et al., PIFM allows this high spectral and lateral resolution with virtually no constraints on sample or substrate properties. [205]

5.6. Tip-Enhanced Raman Spectroscopy

In the conquest of downscaling the possible spatial resolution of Raman imaging, coupling with SPM techniques yielded a chemical mapping resolution with a precision below the diffraction limit of light. In TERS, the enhancement of the Raman scattering signal occurs only at the apex of a near-atomically sharp pin, typically coated with gold or other plasmonically active materials. The SPM probe for TERS is either shaped as a plasmonic nanoantenna or has a plasmonic nanoparticle attached to it. [220] More details can be found in dedicated review articles like those by Zhang et al.^[221] and Deckert-Gaudig et al. [222] In comparison with the absorption techniques at nanoscale discussed in the earlier section, for which the detection scheme is in the near-field, the local effects in the plasmonically enhanced case are observed in the far-field. The SPM is necessary for the positioning and fine control of the nanoantenna, and the feedback loop can be AFM, [223] STM, [224] or tuningfork^[225] based. The free electrons driven by the external electromagnetic field create an evanescent field that strongly enhances the light underneath the tip. Thus, the achievable spatial resolution is mainly affected by the tip diameter and its apex properties. Maximum resolutions obtained so far are below 10 nm including subnanometer resolution.^[203,226,227] The enhancement affects both the incident laser light and the inelastically scattered Raman signal providing optical spectroscopic imaging with resolution below the diffraction limit of light. TERS requires optical components for Raman spectroscopy integrated with an STM/AFM/tuning-fork geometry for its operation. Thus, since its invention in 2000, various TERS setups have been developed, [228] they use bottom-, side-, top- and a parabolic mirror illumination. The most widely used TERS configuration is the side illumination-collection for all feedback systems (STM/AFM/tuning fork).[223,229] The advantage of such a

Thus, despite its benefits, this geometry is not widely used and there are only a few systems in the world (like the one in Zhang-Meixner's group) that can be considered operational. [237,238]

A wide range of materials has been studied with TERS: polymers, [239,240] organic molecules, [203,241] inorganic nanoclusters, [242] nanowires, [243,244], etc. CNTs are one of the materials most well studied with TERS, including the remarkable work of Chen, Hayazawa, and Kawata with STM-TERS to visualize defects in the individual CNTs and the works of Rodriguez, Zahn, and coworkers on identifying and imaging with AFM-TERS carbon allotropes, [245] characterizing defects in the CNT transistors channel, etc. [246] The latter is shown in Figure 10. The representative spectra from several positions in the CNT transistor channel are shown in Figure 10 (bottom left), and the corresponding images on the right side. The G peak intensity image corresponds to the distribution of CNTs in the channel as the G mode at $\approx 1600 \text{ cm}^{-1}$ is a characteristic vibration of the sp²hybridized carbon. The spectra clearly show that some positions have very high D peak intensity and low 2D peak intensity, both a sign of high defect concentration. By following D/G or 2D/G distribution, it is possible to identify the positions where the defect concentration is the highest. By applying other nanoscale characterization methods, such as CS-AFM, it would be possible to correlate the presence of defects to the electrical performance of electronic properties.^[56,246]

One of the current critical research issues in the nanospectroscopy field is the reproducibility of the methods. The efficiency of the plasmonic enhancement of electromagnetic field strongly depends on the minuscule details of the tip apex. The illumination geometry, studied material, and laser power—all these effects affect the final results. Clarifying the role of these parameters helps the experimental reproducibility and our understanding of tip-enhanced methods. This is precisely the topic of an ongoing investigation led by the authors in an interlaboratory study involving over half a dozen groups in Europe.

system is that it has an easy integration and easy operation when compared with the other geometries, it also increases the efficiency of the electric field enhancement by aligning the incident laser polarization along the tip axis. In this geometry, the use of nontransparent samples is possible, including gold- or silver-coated surfaces. In this case, the gap-mode excitation plays an important role in signal enhancement when the tip-sample distance is below 2 nm^[230] improving the sensitivity and the spatial resolution of this technique. This setup has also been modified to suit liquid environments as shown by various groups known as electrochemical TERS (EC-TERS). [231–233]

The second most commonly used technique is top illumination-collection geometry. Herein, the tip is inclined at an obtuse angle, whereas the objective is placed normal to the surface of the sample so that the tip apex is efficiently illuminated from the top. [234] It has higher collection efficiency than side illumination and can be used to study both transparent and nontransparent samples just like the side-illumination geometry. The bottomillumination geometry can only be implemented for transparent samples. Also, a laser illuminates the tip from an objective placed at the bottom of the sample. This setup is not widely used in TERS community due to its sample limitations; however, it has proven to be beneficial to image biological samples. This setup uses AFMbased TERS and a high N.A. objective for the illuminationcollection system. Due to this, the collection efficiency of this setup is highest respective to other geometries. Recent modifications in this geometry for opaque samples have been performed by the Deckert group using a dichroic mirror. [235] A parabolic mirror was developed to increase the collection efficiency of scattered light in all the directions; the first demonstration was described by Steidtner and Pettinger. [236] The setups with parabolic mirror work in a reflection mode, allowing both opaque and transparent samples to be investigated. Just like bottom illumination, the collection efficiency of this setup is higher than the side and top illuminations. The disadvantages of this setup are that it is difficult to integrate the parabolic mirror into commercial STM units, and the optical alignment is a major hindrance to its smooth operation.

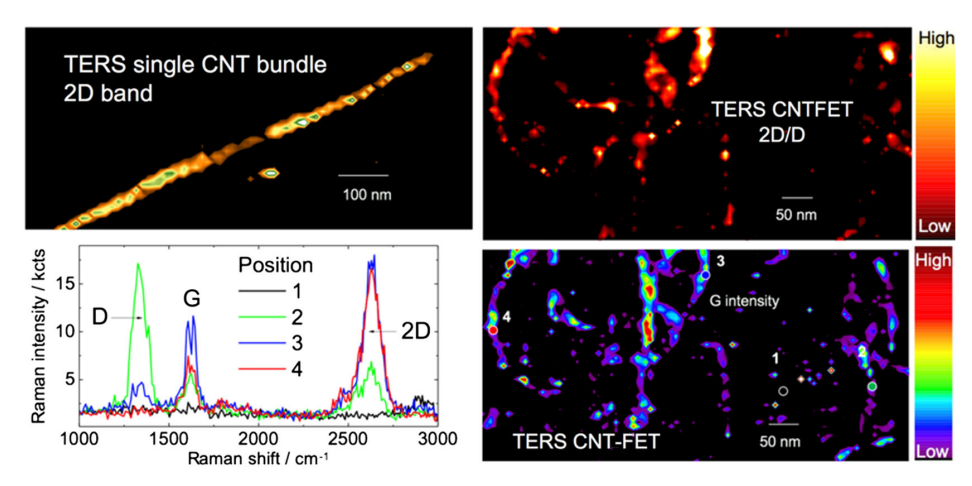


Figure 10. Top left: A TERS image of CNT bundle constructed based on the 2D band intensity. Bottom left: Representative TERS spectra of the CNTs with the signature bands D, G, and 2D marked. The positions 1–4 correspond to the points marked in the bottom right image. Top right: TERS image of the CNT-FET channel constructed based on the 2D/D intensity ratio. Bottom right: TERS map of the G intensity for the same region of the CNT-FET channel. Reproduced with permission.^[247] Copyright 2014, Förderverein für Gerätetechnik und Mikrosystemtechnik Chemnitz e. V.



5.7. New Trends in Advanced Characterization for Detecting Nanoscale Material Quality

In prospect, the combination of TERS imaging and local functionalization can allow the extraction of information not only about the chemical composition but also the nanomaterial quality at the submicrometer length scale. This is a critical point as the correlation of local material quality, material structure (including size and geometry), and material chemistry ultimately defines the properties and function of nanomaterials. Figure 11 shows an artist's view on the usage of TERS with a gold AFM probe. The near-field at the tip enhances the interaction between the incident laser light and the object under investigation, e.g., on single-walled CNTs decorated with Au nanoparticles. Previous studies by Rodriguez et al. focused on the micro-Raman spectroscopy of CNTs in a field-effect transistor configuration[246] and their local functionalization with the gold nanoparticles. [248] Those works show that the nanoparticle decoration of CNTFET channel (consisting of bundles formed by a multitude of CNT chiralities) leads to a change of the radial breathing vibrations that are visible in the local Raman spectrum. The Raman spectroscopy changes can then be attributed to the selective interaction of gold nanoparticles decorating the sidewalls of CNTs of different diameter. This investigation provided a model to evidence changes in CNT upon external perturbations, [249] including accessing the internal bundle structure of CNTs integrated at the CNTFET device level. [250]

6. Conclusion

Aiming at performing nanoscale characterization, the scientific community needs to explore new methods for extracting material properties with a nanometer resolution. AFM-based methods exploit a well-established nanoscale imaging technique offering

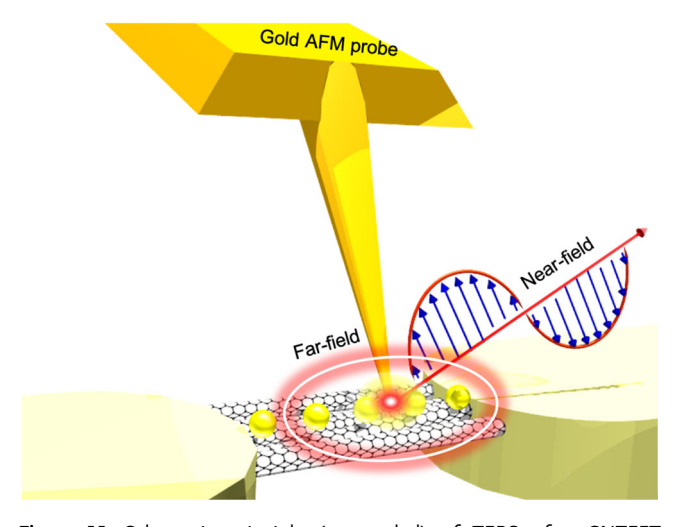


Figure 11. Schematic principle (non-scaled) of TERS of a CNTFET transistor channel decorated with gold nanoparticles. The red-shaded ellipsoid represents the far-field information area (a few μ m²), whereas the smallest region under the tip represents the near-field information area (a few nm²).

great opportunities to study material properties that were not accessible before at the nanoscale with conventional methods.

Electrical properties can be straightforwardly measured using CS-AFM, taking extra care to ensure the reproducibility of the probe that can be affected by the delamination of the metal coating and a high risk of sample contamination. Access to resistivity mapping at the nanoscale also offers new possibilities to test the predictions of quantum-mechanical transport simulations and approximations.

Optoelectronic properties can be accessed by combining local electrical measurements with the scanning-probe techniques that also can access morphologic and mechanical properties under illumination. Examples include photoconductivity as well as KPFM.

Strain and stress investigations at the nanoscale are best performed with TERS. Other techniques like KPFM start to show promise.

Similarly, the chemical composition and material quality at the nanoscale are also characterized by vibrational spectroscopies such as TERS and PTIR. Nanometer resolution is achieved by coupling Raman and IR with scanning probe methods that integrate plasmonic nanoantennas at the end of tips without the loss of information.

As outlined in this study, characterization techniques with nanoscale resolution appear as intermittent glimpses along the advancement track of micro- and nanotechnology. An appropriate combination of existing techniques plays a key role. This research track not only requires interdisciplinary knowledge involving various fields of physical and chemical characterizations but also technical skills in the acquisition, handling, and storage of large data volumes. Furthermore, there are several technological challenges still to be addressed including the harmonization of measurement protocols and the understanding of measurement artifacts arising from the interference between the coupled techniques. The simultaneous investigation of sample topographies in 3D and the chemical and structural mapping made possible by advanced nanocharacterization methods open tremendous opportunities to the development of new materials for the increasingly smart (hybrid and flexible) applications and thus exploit the understanding of the nanoworld as never before.

Acknowledgements

The work was funded by the German Science Foundation (Deutsche Forschungsgemeinschaft, DFG) within the research area DFG FOR 1713 "Sensoric Micro and Nano Systems" and the Federal Cluster of Excellence DFG EXC 1056 "Center for Advancing Electronics Dresden" (cfaed) as well as the European Cooperation in Science and Technology (COST) in the framework of the COST Action MP1302 "Nanospectroscopy." E.S. and R.D.R. thank Tomsk Polytechnic University Competitiveness Enhancement Program for the financial support. The authors also thank D. Stepanishcheva and A. Mukherjee for their help in compiling the manuscript.

Conflict of Interest

The authors declare no conflict of interest.

www.pss-a.com

Keywords

atomic force microscopy, Kelvin probe force microscopy, nanoanalysis, Raman spectroscopy, scanning probe microscopy

> Received: February 7, 2019 Revised: May 11, 2019 Published online: July 22, 2019

- [1] R. Gulotty, M. Castellino, P. Jagdale, A. Tagliaferro, A. A. Balandin, ACS Nano 2013, 7, 5114.
- [2] J. E. Rossi, C. D. Cress, S. M. Goodman, N. D. Cox, I. Puchades, A. R. Bucossi, A. Merrill, B. J. Landi, J. Phys. Chem. C 2016, 120,
- [3] D. Sharma, N. Jaggi, Phys. E 2017, 91, 93.
- [4] Y. Z. Hu, S. W. Koch, D. B. T. Thoai, Mod. Phys. Lett. B 1990, 04,
- [5] F. de Santiago, Á. Miranda, A. Trejo, F. Salazar, E. Carvajal, M. Cruz-Irisson, L. A. Pérez, Int. J. Quantum Chem. 2018, 118, e25713.
- [6] K. Bang, S.-S. Chee, K. Kim, M. Son, H. Jang, B. H. Lee, K. H. Baik, J.-M. Myoung, M.-H. Ham, Nano Convergence 2018, 5, 7.
- [7] S. lijima, Nature 1991, 354, 56.
- [8] S. Iijima, T. Ichihashi, Nature 1993, 363, 603.
- [9] R. Saito, G. Dresselhaus, M. S. Dresselhaus, J. Appl. Phys. 1993, 73,
- [10] L. Chico, V. H. Crespi, L. X. Benedict, S. G. Louie, M. L. Cohen, Phys. Rev. Lett. 1996, 76, 971.
- [11] C. Hierold, T. Helbling, C. Roman, L. Durrer, A. Jungen, C. Stampfer, in Smart Materials & Micro/Nanosystems, Trans Tech Publications 2008, pp. 343-349.
- [12] S. Hartmann, S. Hermann, J. Bonitz, M. Heggen, O. Hölck, A. Shaporin, J. Mehner, S. E. Schulz, T. Gessner, B. Wunderle, Mechatronics 2016, 40, 270.
- [13] P. Meszmer, S. Hahn, K. Hiller, B. Wunderle, Phys. Status Solidi 2019, 15, 1800936.
- [14] M. Muoth, K. Chikkadi, Y. Liu, C. Hierold, in 2013 IEEE 26th International Conference on Micro Electro Mechanical Systems (MEMS), IEEE, 2013, pp. 496-499.
- [15] G. Binnig, H. Rohrer, C. Gerber, E. Weibel, Phys. Rev. Lett. 1982, 49, 57.
- [16] G. Binnig, C. F. Quate, C. Gerber, Phys. Rev. Lett. 1986, 56, 930.
- [17] B. Hecht, B. Sick, U. P. Wild, V. Deckert, R. Zenobi, O. J. F. Martin, D. W. Pohl, J. Chem. Phys. 2000, 112, 7761.
- [18] L. Schermelleh, R. Heintzmann, H. Leonhardt, J. Cell Biol. 2010, 190, 165.
- [19] H. Zhu, J. Fan, J. Du, X. Peng, Acc. Chem. Res. 2016, 49, 2115.
- [20] M. Asakawa, M. Higuchi, G. Mattersteig, T. Nakamura, A. R. Pease, F. M. Raymo, T. Shimizu, J. F. Stoddart, Adv. Mater. 2000, 12, 1099.
- [21] Y. Li, H.-M. Chou, IEEE Trans. Nanotechnol. 2005, 4, 645.
- [22] A. Alexeev, J. Loos, M. M. Koetse, *Ultramicroscopy* **2006**, *106*, 191.
- [23] H. Fiedler, M. Toader, S. Hermann, R. D. Rodriguez, E. Sheremet, M. Rennau, S. Schulze, T. Waechtler, M. Hietschold, D. R. T. Zahn, S. E. Schulz, T. Gessner, ECS J. Solid State Sci. Technol. 2012, 1, M47.
- [24] I. Beinik, B. Galiana, M. Kratzer, C. Teichert, I. Rey-Stolle, C. Algora, P. Tejedor, J. Vac. Sci. Technol. B Microelectron. Nanometer Struct. Process. Meas. Phenom. 2010, 28, C5G5.
- [25] M. Berliocchi, F. Brunetti, A. Di Carlo, P. Lugli, S. Orlanducci, M. L. Terranova, in Proc. of the International Society for Optics and Photonics, SPIE, Bellingham, WA, USA 2003, pp. 633-639.
- [26] M. Berliocchi, S. Orlanducci, A. Reale, P. Regoliosi, A. Di Carlo, P. Lugli, M. L. Terranova, F. Brunetti, G. Bruni, M. Cirillo, Synth. Met. 2004, 145, 171.

- [27] N. Chiodarelli, Y. Li, D. J. Cott, S. Mertens, N. Peys, M. Heyns, S. De Gendt, G. Groeseneken, P. M. Vereecken, Microelectron. Eng. **2011**, 88, 837.
- [28] M. Toader, H. Fiedler, S. Hermann, S. E. Schulz, T. Gessner, M. Hietschold, Nanoscale Res. Lett. 2013, 8, 24.
- [29] S. M. Jafarpour, M. Kini, S. E. Schulz, S. Hermann, Microelectron. Eng. **2017** 167 95
- [30] S. M. Jafarpour, S. E. Schulz, S. Hermann, Diamond Relat. Mater. 2018, 89, 18.
- [31] N. T. Dinh, E. Sowade, T. Blaudeck, S. Hermann, R. D. Rodriguez, D. R. T. Zahn, S. E. Schulz, R. R. Baumann, O. Kanoun, Carbon N. Y. 2016, 96, 382.
- [32] M. Hartmann, R. Schubel, M. Claus, R. Jordan, S. E. Schulz, S. Hermann, Nanotechnology 2018, 29, 035203.
- [33] M. Toader, S. Hermann, L. Scharfenberg, M. Hartmann, M. Mertig, S. E. Schulz, T. Gessner, I. Phys. Chem. C 2016, 120, 10020.
- [34] M. Schröter, M. Claus, S. Hermann, J. Tittmann-Otto, M. Haferlach, S. Mothes, S. Schulz, in 16th Topical Meeting on Silicon Monolithic Integrated Circuits in RF Systems (SiRF), IEEE, Piscataway, NJ, USA 2016, pp. 97-100.
- [35] M. Haferlach, A. Pacheco, P. Sakalas, M. Alexandru, S. Hermann, T. Nardmann, M. Schröter, M. Claus, IEEE Trans. Nanotechnol. 2016. 15. 619.
- [36] C. Ganser, C. Czibula, D. Tscharnuter, T. Schöberl, C. Teichert, U. Hirn, Soft Matter 2017, 14, 140.
- [37] M. Kratzer, M. Lasnik, S. Röhrig, C. Teichert, M. Deluca, Sci. Rep. 2018. 8. 422.
- [38] Wikipedia contributors, Scanning probe microscopy, https://en. wikipedia.org/w/index.php?title=Scanning_probe_microscopy&oldid= 871440181 (accessed: July 2018).
- [39] L. P. Biró, S. D. Lazarescu, P. A. Thiry, A. Fonseca, J. B. Nagy, A. A. Lucas, P. Lambin, Europhys. Lett. 2000, 50, 494.
- [40] F.-X. Zha, G. Bertsche, M. Croitoru, C. Kentsch, S. Roth, D. P. Kern, Carbon N. Y. 2004, 42, 893.
- [41] C. Rabot, S. Clair, Y. Kim, M. Kawai, Jpn. J. Appl. Phys. 2007, 46, 5572.
- [42] P. Lauffer, A. Jung, R. Graupner, A. Hirsch, L. Ley, Phys. Status Solidi B **2006**, 243, 3213.
- [43] R. Strohmaier, C. Ludwig, J. Petersen, B. Gompf, W. Eisenmenger, Surf. Sci. 1996, 351, 292.
- [44] W. Krenner, D. Kühne, F. Klappenberger, J. V. Barth, Sci. Rep. 2013,
- [45] X. He, H. Li, L. Chen, K. Wu, Sci. Rep. 2015, 5, 8830.
- [46] B. Kundu, A. Bera, A. J. Pal, Nanotechnology 2017, 28, 095705.
- [47] G. Paul, B. Kundu, A. J. Pal, Org. Electron. 2018, 59, 27.
- [48] N. Nilius, Surf. Sci. Rep. 2009, 64, 595.
- [49] H.-J. Butt, B. Cappella, M. Kappl, Surf. Sci. Rep. 2005, 59, 1.
- [50] R. García, Surf. Sci. Rep. 2002, 47, 197.
- [51] S. NanoWorld AG, Electrical AFM Probes (EFM, SCM, Tuna, SSRM) from NanoWorld, https://www.nanoworld.com/electricalafm-tips (accessed: July 2019).
- [52] A. Carruthers, J. Carruthers, Skin Therapy Lett. 2008, 13, 1.
- [53] B. Bhushan, H. Fuchs, M. Tomitori, Applied Scanning Probe Methods VIII: Scanning Probe Microscopy Techniques, Springer, Berlin, Heidelberg 2007.
- [54] B. Bhushan, H. Fuchs, M. Tomitori, Eds., Applied Scanning Probe Methods VIII: Scanning Probe Microscopy Techniques, Springer, Berlin, Heidelberg 2008.
- [55] Agilent Technologies Inc., Agilent Technologies 5600LS Scanning Probe Microscope User's Guide, Palo Alto, CA, USA 2013.
- [56] H. Fiedler, M. Toader, S. Hermann, R. D. Rodriguez, E. Sheremet, M. Rennau, S. Schulze, T. Waechtler, M. Hietschold, D. R. T. Zahn, S. E. Schulz, T. Gessner, Microelectron. Eng. 2014, 120, 210.

- [57] F. Teichert, A. Zienert, J. Schuster, M. Schreiber, New J. Phys. 2014, 16, 123026.
- [58] F. Teichert, A. Zienert, J. Schuster, M. Schreiber, Comput. Mater. Sci. 2017, 138, 49.
- [59] F. Teichert, A. Zienert, J. Schuster, M. Schreiber, J. Comput. Phys. 2017, 334, 607.
- [60] A. Fediai, D. A. Ryndyk, G. Seifert, S. Mothes, M. Claus, M. Schröter, G. Cuniberti. Nanoscale 2016. 8, 10240.
- [61] A. Zienert, J. Schuster, T. Gessner, Nanotechnology 2014, 25, 425203.
- [62] M. Toader, H. Fiedler, M. Hietschold, Annual Report of the Fraunhofer ENAS, Chemnitz, Germany 2011.
- [63] F. Tuinstra, J. L. Koenig, J. Compos. Mater. 1970, 4, 492.
- [64] M. S. Dresselhaus, A. Jorio, M. Hofmann, G. Dresselhaus, R. Saito, Nano Lett. 2010, 10, 751.
- [65] M. M. Lucchese, F. Stavale, E. H. Martins Ferreira, C. Vilani, M. V. O. Moutinho, R. B. Capaz, C. A. Achete, A. Jorio, Carbon N. Y. 2010, 48, 1592.
- [66] A. Eckmann, A. Felten, A. Mishchenko, L. Britnell, R. Krupke, K. S. Novoselov, C. Casiraghi, *Nano Lett.* 2012, 12, 3925.
- [67] H. Fiedler, S. Hermann, S. E. Schulz, T. Gessner, in Int. Interconnect Technology Conf., IEEE, Piscataway, NJ, USA 2011, pp. 1–3.
- [68] H. Fiedler, M. Toader, S. Hermann, M. Rennau, R. D. Rodriguez, E. Sheremet, M. Hietschold, D. R. T. Zahn, S. E. Schulz, T. Gessner, *Microelectron. Eng.* 2015, 137, 130.
- [69] M. Nonnenmacher, M. P. O'Boyle, H. K. Wickramasinghe, Appl. Phys. Lett. 1991, 58, 2921.
- [70] W. Melitz, J. Shen, A. C. Kummel, S. Lee, Surf. Sci. Rep. 2011, 66, 1.
- [71] I. Bdikin, D. K. Sharma, G. Otero-Irurueta, M. J. Hortigüela, P. K. Tyagi, V. Neto, M. K. Singh, Appl. Mater. Today 2017, 8, 18.
- [72] S. Sadewasser, T. Glatzel, Kelvin Probe Force Microscopy: Measuring and Compensating Electrostatic Forces, Springer, Berlin Heidelberg 2011
- [73] S. Sadewasser, T. Glatzel, Kelvin Probe Force Microscopy: From Single Charge Detection to Device Characterization, Springer, Berlin Heidelberg 2018.
- [74] S. Sadewasser, T. Glatzel, Kelvin Probe Force Microscopy: Measuring and Compensating Electrostatic Forces, Springer, Berlin Heidelberg 2011.
- [75] A. Liscio, V. Palermo, D. Gentilini, F. Nolde, K. Müllen, P. Samorì, Adv. Funct. Mater. 2006, 16, 1407.
- [76] H. O. Jacobs, H. F. Knapp, A. Stemmer, Rev. Sci. Instrum. 1999, 70, 1756.
- [77] U. Zerweck, C. Loppacher, T. Otto, S. Grafström, L. M. Eng, Phys. Rev. B 2005, 71, 125424.
- [78] T. Glatzel, S. Sadewasser, M. C. Lux-Steiner, Appl. Surf. Sci. 2003, 210, 84
- [79] E. J. Spadafora, K. Saint-Aubin, C. Celle, R. Demadrille, B. Grévin, J.-P. Simonato, Carbon N. Y. 2012, 50, 3459.
- [80] M. Tortonese, IEEE Eng. Med. Biol. Mag. 1997, 16, 28.
- [81] P. Brodard, M. Bechelany, L. Philippe, J. Michler, J. Raman Spectrosc. 2012, 43, 745.
- [82] C. C. Yuan, D. Zhang, Y. Gan, Rev. Sci. Instrum. 2017, 88, 031101.
- [83] P. Walke, Y. Fujita, W. Peeters, S. Toyouchi, W. Frederickx, S. De Feyter, H. Uji-I, Nanoscale 2018, 10, 7556.
- [84] X. Ma, Y. Zhu, N. Yu, S. Kim, Q. Liu, L. Apontti, D. Xu, R. Yan, M. Liu, Nano Lett. 2018, 19, 100, DOI: 10.1021/acs.nanolett.8b03399.
- [85] R. D. Rodriguez, A. Anne, E. Cambril, C. Demaille, *Ultramicroscopy* 2011, 111, 973.
- [86] V. Snitka, R. D. Rodriguez, V. Lendraitis, Microelectron. Eng. 2011, 88, 2759
- [87] V. A. Kolchuzhin, E. Sheremet, K. Bhattacharya, R. D. Rodriguez, S. D. Paul, J. Mehner, M. Hietschold, D. R. T. Zahn, *Mechatronics* 2016, 40, 281.

- [88] M. Freitag, Y. Martin, J. A. Misewich, R. Martel, P. Avouris, Nano Lett. 2003, 3, 1067.
- [89] P. Avouris, MRS Bull. 2004, 29, 403.
- [90] P. Avouris, M. Freitag, V. Perebeinos, Nat. Photonics 2008, 2, 341.
- [91] B. Mahler, L. Guillemot, L. Bossard-Giannesini, S. Ithurria, D. Pierucci, A. Ouerghi, G. Patriarche, R. Benbalagh, E. Lacaze, F. Rochet, E. Lhuillier, J. Phys. Chem. C 2016, 120, 12351.
- [92] J. Kim, K.-B. Song, Micron 2007, 38, 409.
- [93] A. Bouhelier, in Reference Module in Materials Science and Materials Engineering, Elsevier, Amsterdam 2016.
- [94] S. Kirstein, Curr. Opin. Colloid Interface Sci. 1999, 4, 256.
- [95] R. Hillenbrand, T. Taubner, F. Keilmann, Nature 2002, 418, 159.
- [96] F. Huth, A. Govyadinov, S. Amarie, W. Nuansing, F. Keilmann, R. Hillenbrand, Nano Lett. 2012, 12, 3973.
- [97] A. A. Govyadinov, I. Amenabar, F. Huth, P. S. Carney, R. Hillenbrand, J. Phys. Chem. Lett. 2013, 4, 1526.
- [98] N. Mauser, A. Hartschuh, Chem. Soc. Rev. 2014, 43, 1248.
- [99] D. Nowak, W. Morrison, H. K. Wickramasinghe, J. Jahng, E. Potma, L. Wan, R. Ruiz, T. R. Albrecht, K. Schmidt, J. Frommer, D. P. Sanders, S. Park, Sci. Adv. 2016, 2, e1501571.
- [100] F. De Angelis, R. P. Zaccaria, E. Di Fabrizio, Opt. Express 2012, 20, 29626.
- [101] A. Jarzembski, C. Shaskey, K. Park, Front. Energy Power Eng. Chin. 2018, 12, 43.
- [102] M. S. Marcus, J. M. Simmons, O. M. Castellini, R. J. Hamers, M. A. Eriksson, J. Appl. Phys. 2006, 100, 084306.
- [103] M. Engel, K. E. Moore, A. Alam, S. Dehm, R. Krupke, B. S. Flavel, ACS Nano 2014, 8, 9324.
- [104] S.-W. Chang, J. Theiss, J. Hazra, M. Aykol, R. Kapadia, S. B. Cronin, Appl. Phys. Lett. 2015, 107, 053107.
- [105] Time-Resolved Photocurrent Mapping, https://www.parksystems. com/index.php/park-spm-modes/94-electrical-properties/243-time-resolved-photocurrent-mapping (accessed: May 2019).
- [106] N. Rauhut, M. Engel, M. Steiner, R. Krupke, P. Avouris, A. Hartschuh, ACS Nano 2012, 6, 6416.
- [107] C. Karnetzky, L. Sponfeldner, M. Engl, A. W. Holleitner, Phys. Rev. B 2017, 95, 161405, DOI: 10.1103/PhysRevB.95.161405.
- [108] J. Quereda, T. S. Ghiasi, F. A. van Zwol, C. H. van der Wal, B. J. van Wees, 2D Mater. 2017, 5, 015004.
- [109] S. Khasminskaya, F. Pyatkov, B. S. Flavel, W. H. Pernice, R. Krupke, Adv. Mater. 2014. 26. 3465.
- [110] F. Pyatkov, V. Fütterling, S. Khasminskaya, B. S. Flavel, F. Hennrich, M. M. Kappes, R. Krupke, W. H. P. Pernice, *Nat. Photonics* 2016, 10, 420.
- [111] S. Khasminskaya, F. Pyatkov, K. Słowik, S. Ferrari, O. Kahl, V. Kovalyuk, P. Rath, A. Vetter, F. Hennrich, M. M. Kappes, G. Gol'tsman, A. Korneev, C. Rockstuhl, R. Krupke, W. H. P. Pernice, Nat. Photonics 2016, 10, 727.
- [112] A. De Sanctis, J. D. Mehew, M. F. Craciun, S. Russo, *Materials* 2018, 11, 1762, DOI: 10.3390/ma11091762.
- [113] M. Nonnenmacher, J. Greschner, O. Wolter, R. Kassing, J. Vac. Sci. Technol., B Microelectron. Nanometer Struct. –Process., Meas., Phenom. 1991, 9, 1358.
- [114] X. Sun, X. Wang, P. Wang, B. Sheng, M. Li, J. Su, J. Zhang, F. Liu, X. Rong, F. Xu, X. Yang, Z. Qin, W. Ge, B. Shen, Opt. Mater. Express OME 2017, 7, 904.
- [115] Z. Schumacher, Y. Miyahara, A. Spielhofer, P. Grutter, *Phys. Rev. Appl.* 2016, 5, 044018.
- [116] K. Prashanthi, R. Gaikwad, T. Thundat, Nanotechnology 2013, 24, 505710
- [117] F. Streicher, S. Sadewasser, M. C. Lux-Steiner, Rev. Sci. Instrum. 2009, 80, 013907.





www.pss-a.com

- [118] E. N. Kaya, T. Basova, M. Polyakov, M. Durmuş, B. Kadem, A. Hassan, RSC Adv. 2015, 5, 91855.
- [119] R. Chitta, A. S. D. Sandanayaka, A. L. Schumacher, L. D'Souza, Y. Araki, O. Ito, F. D'Souza, J. Phys. Chem. C 2007, 111, 6947.
- [120] T. Assmus, K. Balasubramanian, M. Burghard, K. Kern, M. Scolari, N. Fu, A. Myalitsin, A. Mews, Appl. Phys. Lett. 2007, 90, 173109.
- [121] N. Lalaoui, P. Rousselot-Pailley, V. Robert, Y. Mekmouche, R. Villalonga, M. Holzinger, S. Cosnier, T. Tron, A. Le Goff, ACS Catal. 2016, 6, 1894.
- [122] A. M. Elliott, O. S. Ivanova, C. B. Williams, T. A. Campbell, Adv. Eng. Mater. 2013, 17, 903, DOI: 10.1002/adem.201300020.
- [123] E. Katzir, S. Yochelis, Y. Paltiel, S. Azoubel, A. Shimoni, S. Magdassi, Sens. Actuators B Chem. 2014, 196, 112.
- [124] M. Hartwig, R. Zichner, Y. Joseph, Chemosensors 2018, 6, 66.
- [125] M. Mahjouri-Samani, Y. S. Zhou, X. N. He, W. Xiong, P. Hilger, Y. F. Lu, *Nanotechnology* **2013**, *24*, 035502.
- [126] D. J. Norris, M. G. Bawendi, Phys. Rev. B 1996, 53, 16338.
- [127] E. A. Weiss, R. C. Chiechi, S. M. Geyer, V. J. Porter, D. C. Bell, M. G. Bawendi, G. M. Whitesides, J. Am. Chem. Soc. 2008, 130, 74.
- [128] T. Blaudeck, E. I. Zenkevich, F. Cichos, C. von Borczyskowski, I. Phys. Chem. C 2008, 112, 20251.
- [129] E. I. Zenkevich, T. Blaudeck, A. Milekhin, C. von Borczyskowski, Int. J. Spectrosc. 2011, 2012, 14, DOI 10.1155/2012/971791.
- [130] M. M. Alvarez, J. T. Khoury, T. G. Schaaff, M. N. Shafigullin, I. Vezmar, R. L. Whetten, J. Phys. Chem. B 1997, 101, 3706.
- [131] K.-S. Lee, M. A. El-Sayed, J. Phys. Chem. B 2006, 110, 19220.
- [132] A. Narayanaswamy, L. F. Feiner, A. Meijerink, P. J. van der Zaag, ACS Nano 2009, 3, 2539.
- [133] S. A. Empedocles, R. Neuhauser K. Shimizu M. G. Bawendi, Adv. Mater. 1999, 11, 1214, DOI: 10.1002/(SICI)1521-4095(199910)11:14.
- [134] E. P. Petrov, F. Cichos, E. Zenkevich, D. Starukhin, C. von Borczyskowski, Chem. Phys. Lett. 2005, 402, 233.
- [135] S. Deshpande, J. Heo, A. Das, P. Bhattacharya, *Nat. Commun.* 2013, 4, 1675.
- [136] M. Kumar, A. Dubey, K. M. Reza, N. Adhikari, Q. Qiao, V. Bommisetty, Phys. Chem. Chem. Phys. 2015, 17, 27690.
- [137] M. Goldsche, J. Sonntag, T. Khodkov, G. J. Verbiest, S. Reichardt, C. Neumann, T. Ouaj, N. von den Driesch, D. Buca, C. Stampfer, Nano Lett. 2018, 18, 1707.
- [138] R. Ramachandramoorthy, A. Beese, H. Espinosa, Int. J. Mech. Sci. 2018, 149, 452.
- [139] P. Meszmer, R. D. Rodriguez, E. Sheremet, D. R. T. Zahn, B. Wunderle, Microelectron. Reliab. 2017, 79, 104.
- [140] I. D. Wolf, Semicond. Sci. Technol. 1996, 11, 139.
- [141] L. A. Starman, J. A. Lott, M. S. Amer, W. D. Cowan, J. D. Busbee, Sens. Actuators A: Phys. 2003, 104, 107.
- [142] O. Perroud, R. Vayrette, C. Rivero, O. Thomas, J.-S. Micha, O. Ulrich, Microelectron. Eng. 2010, 87, 394.
- [143] S. Hartmann, H. Sturm, T. Blaudeck, O. Hölck, S. Hermann, S. E. Schulz, T. Gessner, B. Wunderle, J. Mater. Sci. 2016, 51, 1217.
- [144] A. J. Wilkinson, Ultramicroscopy 1996, 62, 237.
- [145] A. Czyzak, J. Z. Domagala, G. Maciejewski, Z. R. Zytkiewicz, Appl. Phys. A: Mater. Sci. Process. 2008, 91, 601.
- [146] Z. Q. Li, C. J. Lu, Z. P. Xia, Y. Zhou, Z. Luo, *Carbon N. Y.* **2007**, 45,
- [147] U. Zschenderlein, D. Vogel, E. Auerswald, O. Hölck, H. Rajendran, P. Ramm, R. Pufall, B. Wunderle, in 64th Electronic Components and Technology Conf. (ECTC), IEEE, Piscataway, NJ, USA 2014, pp. 1134–1142.
- [148] American Society for Metals, ASM Handbook: Properties and Selection: Nonferrous Alloys and Special-Purpose Materials, ASM International, Handbook Committee, Russell, OH, USA 1992.

- [149] E. Langer, S. Däbritz, C. Schurig, W. Hauffe, Appl. Surf. Sci. 2001, 179, 45.
- [150] J. Bauch, J. Brechbühl, H. -J. Ullrich, G. Meinl, H. Lin, W. Kebede, Cryst. Res. Technol. 1999, 34, 71.
- [151] J. I. Goldstein, D. E. Newbury, J. R. Michael, N. W. M. Ritchie, J. H. J. Scott, D. C. Joy, Scanning Electron Microscopy and X-Ray Microanalysis, Springer, Russell, OH, USA 2017.
- [152] M. J. McLean, W. A. Osborn, Ultramicroscopy 2018, 185, 21.
- [153] N. Schäfer, A. J. Wilkinson, T. Schmid, A. Winkelmann, G. A. Chahine, T. U. Schülli, T. Rissom, J. Marquardt, S. Schorr, D. Abou-Ras, *Ultramicroscopy* 2016, 169, 89.
- [154] A. J. Wilkinson, G. Meaden, D. J. Dingley, *Ultramicroscopy* 2006, 106, 307
- [155] E. G. McRae, R. A. Malic, Surf. Sci. Lett. 1985, 163, L702.
- [156] C. Berger, Z. Song, T. Li, X. Li, A. Y. Ogbazghi, R. Feng, Z. Dai, A. N. Marchenkov, E. H. Conrad, P. N. First, W. A. de Heer, *I. Phys. Chem. B* 2004, 108, 19912.
- [157] N. Sabate, D. Vogel, A. Gollhardt, J. Keller, C. Cane, I. Gracia, J. R. Morante, B. Michel, J. Microelectromech. Syst. 2007, 16, 365.
- [158] D. Vogel, I. Maus, B. Michel, in 3rd Electronics System Integration Technology Conf., IEEE, Piscataway, NJ, USA 2010, pp. 1-5.
- [159] C. R. B. Álvarez, M. L. Aranda, A. T. Jacome, W. C. Arriaga, J. de la Hidalga Wade, in 2016 13th Int. Conf. on Electrical Engineering, Computing Science and Automatic Control (CCE) 2016, pp. 1–6.
- [160] L. Elbrecht, U. Storm, R. Catanescu, J. Binder, J. Micromech. Microeng. 1999, 7, 151.
- [161] G. Schiavone, J. Murray, S. Smith, M. P. Y. Desmulliez, A. R. Mount, A. J. Walton, J. Micromech. Microeng. 2016, 26, 095013.
- [162] B. A. Mathe, J. D. Comins, A. G. Every, L. W. Hobbs, AIP Adv. 2017, 7, 025108.
- [163] C. V. Raman, K. S. Krishnan, Nature 1928, 121, 501.
- [164] I. D. Wolf, I. De Wolf, J. Raman Spectrosc. 1999, 30, 877.
- [165] S. J. Harris, A. E. O'Neill, W. Yang, P. Gustafson, J. Boileau, W. H. Weber, B. Majumdar, S. Ghosh, J. Appl. Phys. 2004, 96, 7195.
- [166] S. Narayanan, S. R. Kalidindi, L. S. Schadler, J. Appl. Phys. 1997, 82, 2595
- [167] E. Anastassakis, A. Cantarero, M. Cardona, Phys. Rev. B 1990, 41, 7529.
- [168] M. Chandrasekhar, J. B. Renucci, M. Cardona, Phys. Rev. B 1978, 17, 1623.
- [169] V. T. Srikar, A. K. Swan, M. S. Unlu, B. B. Goldberg, S. M. Spearing, I. Microelectromech. Syst. 2003, 12, 779.
- [170] X. Wu, J. Yu, T. Ren, L. Liu, Microelectron. J. 2007, 38, 87.
- [171] T.-A. Yano, T. Ichimura, S. Kuwahara, F. H'dhili, K. Uetsuki, Y. Okuno, P. Verma, S. Kawata, Nat. Commun. 2013, 4, 2592.
- [172] M. Rahaman, R. D. Rodriguez, G. Plechinger, S. Moras, C. Schüller, T. Korn, D. R. T. Zahn, Nano Lett. 2017, 17, 6027.
- [173] R. Beams, L. G. Cançado, A. Jorio, A. N. Vamivakas, L. Novotny, Nanotechnology 2015, 26, 175702.
- [174] Y. Ogawa, T. Toizumi, F. Minami, A. V. Baranov, *Phys. Rev. B* 2011, 83, 081302, DOI: 10.1103/physrevb.83.081302.
- [175] K. Unal, H. K. Wickramasinghe, Appl. Phys. Lett. 2007, 90, 113111.
- [176] K. Gajewski, S. Goniszewski, A. Szumska, M. Moczała, P. Kunicki, J. Gallop, N. Klein, L. Hao, T. Gotszalk, *Diamond Relat. Mater.* 2016, 64, 27.
- [177] I. Schmitz, M. Schreiner, G. Friedbacher, M. Grasserbauer, Appl. Surf. Sci. 1997, 115, 190.
- [178] R. García, R. Pérez, Surf. Sci. Rep. 2002, 47, 197.
- [179] M. A. Bañares, M. Olga Guerrero-Pérez, J. L. G. Fierro, G. G. Cortez, J. Mater. Chem. 2002, 12, 3337.
- [180] H. J. Cortes, B. Winniford, J. Luong, M. Pursch, J. Sep. Sci. 2009, 32, 883





- [181] D. Guillarme, J. Ruta, S. Rudaz, J.-L. Veuthey, Anal. Bioanal. Chem. 2010, 397, 1069.
- [182] A. J. R. Heck, R. H. H. Van Den Heuvel, Mass Spectrom. Rev. 2004, 23, 368.
- [183] H. Egge, J. Peter-Katalinić, Mass Spectrom. Rev. 1987, 6, 331.
- [184] A. G. Harrison, Chemical Ionization Mass Spectrometry, 2nd Ed., Taylor & Francis, London 2017.
- [185] C. Fenselau, P. A. Demirev, Mass Spectrom. Rev. 2001, 20, 157.
- [186] R. L. Hansen, Y. J. Lee, Chem. Rec. 2018, 18, 65.
- [187] M. E. Dueñas, A. D. Feenstra, A. R. Korte, P. Hinners, Y. J. Lee, in Methods in Molecular Biology, Springer, Heidelberg 2017, pp. 217– 231
- [188] M. M. Gessel, J. L. Norris, R. M. Caprioli, J. Proteomics 2014, 107, 71.
- [189] S. Stankovich, D. A. Dikin, R. D. Piner, K. A. Kohlhaas, A. Kleinhammes, Y. Jia, Y. Wu, S. T. Nguyen, R. S. Ruoff, *Carbon N. Y.* 2007, 45, 1558.
- [190] K. Krishnamoorthy, M. Veerapandian, K. Yun, S.-J. Kim, *Carbon N. Y.* 2013, 53, 38.
- [191] A. C. Ferrari, D. M. Basko, Nat. Nanotechnol. 2013, 8, 235.
- [192] G. Viera, S. Huet, L. Boufendi, J. Appl. Phys. 2001, 90, 4175.
- [193] F. Rosi, A. Federici, B. G. Brunetti, A. Sgamellotti, S. Clementi, C. Miliani, Anal. Bioanal. Chem. 2011, 399, 3133.
- [194] M. Diem, M. Romeo, S. Boydston-White, M. Miljković, C. Matthäus, Analyst 2004, 129, 880.
- [195] E. Abbe Hon, J. Royal Microsc. Soc. 1881, 1, 388.
- [196] A. Feofanov, S. Sharonov, P. Valisa, E. Da Silva, I. Nabiev, M. Manfait, Rev. Sci. Instrum. 1995, 66, 3146.
- [197] M. J. Matthews, J. W. P. Hsu, S. Gu, T. F. Kuech, Appl. Phys. Lett. 2001, 79, 3086.
- [198] D. R. Mason, M. V. Jouravlev, K. S. Kim, Opt. Lett. 2010, 35, 2007.
- [199] X. Zhang, Z. Liu, Nat. Mater. 2008, 7, 435.
- [200] D. Gatto Monticone, K. Katamadze, P. Traina, E. Moreva, J. Forneris, I. Ruo-Berchera, P. Olivero, I. P. Degiovanni, G. Brida, M. Genovese, Phys. Rev. Lett. 2014, 113, 143602.
- [201] A. Shemer, D. Mendlovic, Z. Zalevsky, J. Garcia, P. Garcia Martinez, Appl. Opt. 1999, 38, 7245.
- [202] V. Micó, Z. Zalevsky, C. Ferreira, J. García, Opt. Express 2008, 16, 19260.
- [203] R. Zhang, Y. Zhang, Z. C. Dong, S. Jiang, C. Zhang, L. G. Chen, L. Zhang, Y. Liao, J. Aizpurua, Y. Luo, J. L. Yang, J. G. Hou, *Nature* 2013, 498, 82.
- [204] A. Dazzi, R. Prazeres, F. Glotin, J. M. Ortega, Opt. Lett. 2005, 30, 2388.
- [205] R. A. Murdick, W. Morrison, D. Nowak, T. R. Albrecht, J. Jahng, S. Park, *Jpn. J. Appl. Phys.* **2017**, *56*, 08LA04.
- [206] F. Lu, M. Jin, M. A. Belkin, Nat. Photonics 2014, 8, 307.
- [207] R. D. Rodriguez, T. I. Madeira, E. Sheremet, E. Bortchagovsky, A. Mukherjee, M. Hietschold, D. R. T. Zahn, ACS Photonics 2018, 5, 3338.
- [208] A. Dazzi, C. B. Prater, Q. Hu, D. B. Chase, J. F. Rabolt, C. Marcott, Appl. Spectrosc. 2012, 66, 1365.
- [209] C. Mayet, A. Dazzi, R. Prazeres, F. Allot, F. Glotin, J. M. Ortega, Opt. Lett. 2008, 33, 1611.
- [210] A. Dazzi, in Thermal Nanosystems and Nanomaterials (Ed: S. Volz), Springer, Berlin, Heidelberg 2009, pp. 469–503.
- [211] P.-O. Chapuis, in Quantitative Data Processing in Scanning Probe Microscopy, Elsevier, Amsterdam 2018, pp. 303–332.
- [212] A. Hammiche, H. M. Pollock, M. Reading, M. Claybourn, P. H. Turner, K. Jewkes, Appl. Spectrosc. 1999, 53, 810.
- [213] M. Reading, D. M. Price, D. B. Grandy, R. M. Smith, L. Bozec, M. Conroy, A. Hammiche, H. M. Pollock, *Macromol. Symp.* 2001, 167, 45.

- [214] J. R. Felts, H. Cho, M.-F. Yu, L. A. Bergman, A. F. Vakakis, W. P. King, Rev. Sci. Instrum. 2013, 84, 023709.
- [215] W. I. Gruszecki, A. J. Kulik, E. Janik, J. Bednarska, R. Luchowski, W. Grudzinski, G. Dietler, *Nanoscale* 2015, 7, 14659.
- [216] I. Rajapaksa, K. Uenal, H. K. Wickramasinghe, Appl. Phys. Lett. 2010, 97, 073121.
- [217] J. Jahng, F. T. Ladani, R. M. Khan, E. O. Potma, in Proc. International Society for Optics and Photonics, SPIE, Bellingham, WA, USA 2016.
- [218] T. U. Tumkur, X. Yang, B. Cerjan, N. J. Halas, P. Nordlander, I. Thomann, *Nano Lett.* **2016**, *16*, 7942.
- [219] M. Rajaei, M. A. Almajhadi, J. Zeng, H. K. Wickramasinghe, Opt. Express 2018, 26, 26365.
- [220] J. Wessel, J. Opt. Soc. Am. B 1985, 2, 1538.
- [221] Z. Zhang, S. Sheng, R. Wang, M. Sun, Anal. Chem. 2016, 88, 9328.
- [222] T. Deckert-Gaudig, A. Taguchi, S. Kawata, V. Deckert, Chem. Soc. Rev. 2017, 46, 4077.
- [223] R. M. Stöckle, Y. D. Suh, V. Deckert, R. Zenobi, Chem. Phys. Lett. 2000, 318, 131.
- [224] C. Chen, N. Hayazawa, S. Kawata, Nat. Commun. 2014, 5, 3312.
- [225] C. C. Neacsu, J. Dreyer, N. Behr, M. B. Raschke, *Phys. Rev. B* 2006, 73, 193406.
- [226] A. Hartschuh, Angew. Chem., Int. Ed. 2008, 47, 8178.
- [227] T. Ichimura, S. Fujii, P. Verma, T. Yano, Y. Inouye, S. Kawata, *Phys. Rev. Lett.* 2009, 102, 186101.
- [228] X. Wang, S.-C. Huang, T.-X. Huang, H.-S. Su, J.-H. Zhong, Z.-C. Zeng, M.-H. Li, B. Ren, Chem. Soc. Rev. 2017, 46, 4020.
- [229] N. Hayazawa, Y. Inouye, Z. Sekkat, S. Kawata, Opt. Commun. 2000, 183, 333.
- [230] A. Downes, D. Salter, A. Elfick, J. Phys. Chem. B 2006, 110, 6692.
- [231] N. Martín Sabanés, T. Ohto, D. Andrienko, Y. Nagata, K. F. Domke, Angew. Chem., Int. Ed. 2017, 56, 9796.
- [232] Z.-C. Zeng, S.-C. Huang, D.-Y. Wu, L.-Y. Meng, M.-H. Li, T.-X. Huang, J.-H. Zhong, X. Wang, Z.-L. Yang, B. Ren, J. Am. Chem. Soc. 2015, 137, 11928.
- [233] D. Kurouski, M. Mattei, R. P. Van Duyne, Nano Lett. 2015, 15, 7956.
- [234] K. L. A. Chan, S. G. Kazarian, Nanotechnology 2011, 22, 175701.
- [235] T. Deckert-Gaudig, M. Richter, D. Knebel, T. Jähnke, T. Jankowski, E. Stock, V. Deckert, Appl. Spectrosc. 2014, 68, 916.
- [236] J. Steidtner, B. Pettinger, Phys. Rev. Lett. 2008, 100, 236101.
- [237] C. Stanciu, M. Sackrow, A. J. Meixner, J. Microsc. 2008, 229, 247.
- [238] A. Horneber, K. Braun, J. Rogalski, P. Leiderer, A. J. Meixner, D. Zhang, Phys. Chem. Chem. Phys. 2015, 17, 21288.
- [239] B.-S. Yeo, E. Amstad, T. Schmid, J. Stadler, R. Zenobi, Small 2009, 5, 952.
- [240] L. Xue, W. Li, G. G. Hoffmann, J. G. P. Goossens, J. Loos, G. de With, Macromolecules 2011, 44, 2852.
- [241] A. B. Zrimsek, N. Chiang, M. Mattei, S. Zaleski, M. O. McAnally, C. T. Chapman, A.-I. Henry, G. C. Schatz, R. P. Van Duyne, *Chem. Rev.* 2017, 117, 7583.
- [242] A. K. Sivadasan, A. Patsha, A. Maity, T. K. Chini, S. Dhara, J. Phys. Chem. C 2017, 121, 26967.
- [243] M. Becker, V. Sivakov, G. Andrä, R. Geiger, J. Schreiber, S. Hoffmann, J. Michler, A. P. Milenin, P. Werner, S. H. Christiansen, Nano Lett. 2007, 7, 75.
- [244] A. Patsha, S. Dhara, A. K. Tyagi, Appl. Phys. Lett. 2015, 107, 123108.
- [245] E. Sheremet, R. D. Rodriguez, A. L. Agapov, A. P. Sokolov, M. Hietschold, D. R. T. Zahn, *Carbon N. Y.* **2016**, *96*, 588.
- [246] R. D. Rodriguez, M. Toader, S. Hermann, E. Sheremet, S. Müller, O. D. Gordan, H. Yu, S. E. Schulz, M. Hietschold, D. R. T. Zahn, Nanoscale Res. Lett. 2012, 7, 682.
- [247] E. Sheremet, R. D. Rodriguez, J. Kalbacova, M. Hietschold, D. R. T. Zahn, in 12. Chemnitzer Fachtagung Mikrosystemtechnik, Chemnitz, Germany 2014.





- [248] T. Blaudeck, D. Adner, S. Hermann, H. Lang, T. Gessner, S. E. Schulz, Microelectron. Eng. 2015, 137, 135.
- [249] R. D. Rodriguez, B. Ma, E. Sheremet, Phys. Status Solidi 2018, 89, 1800412.
- [250] R. D. Rodriguez, T. Blaudeck, J. Kalbacova, E. Sheremet, S. Schulze, D. Adner, S. Hermann, M. Hietschold, H. Lang, S. E. Schulz, D. R. T. Zahn, RSC Adv. 2016, 6, 15753.